

Probing 2D Asymmetries of an Exoplanet Atmosphere from Chromatic Transit Variation

SHOTARO TADA ¹, HAJIME KAWAHARA ^{2,3}, YUI KAWASHIMA ^{4,5,6,2,7}, TAKAYUKI KOTANI ^{8,1,9} AND
KENTO MASUDA ¹⁰

¹Graduate University for Advanced Studies, SOKENDAI, 2-21-1 Osawa, Mitaka, Tokyo 181-8588, Japan

²Institute of Space and Astronautical Science, Japan Aerospace Exploration Agency, 3-1-1 Yoshinodai, Chuo-ku, Sagami-hara, Kanagawa 252-5210, Japan

³Department of Astronomy, Graduate School of Science, The University of Tokyo, 7-3-1 Hongo, Bunkyo-ku, Tokyo 113-0033, Japan

⁴Department of Astronomy, Graduate School of Science, Kyoto University, Kitashirakawa Oiwake-cho, Sakyo-ku, Kyoto 606-8502, Japan

⁵Frontier Research Institute for Interdisciplinary Sciences, Tohoku University, 6-3 Aramaki aza Aoba, Aoba-ku, Sendai, Miyagi 980-8578, Japan

⁶Department of Geophysics, Graduate School of Science, Tohoku University, 6-3 Aramaki aza Aoba, Aoba-ku, Sendai, Miyagi 980-8578, Japan

⁷Cluster for Pioneering Research, RIKEN, 2-1 Hirosawa, Wako, Saitama 351-0198, Japan

⁸Astrobiology Center, 2-21-1 Osawa, Mitaka, Tokyo 181-8588, Japan

⁹National Astronomical Observatory of Japan, 2-21-1 Osawa, Mitaka, Tokyo 181-8588, Japan

¹⁰Department of Earth and Space Science, Graduate School of Science, Osaka University, 1-1 Machikaneyama-cho, Toyonaka, Osaka 560-0043, Japan

ABSTRACT

We propose a new method for investigating atmospheric inhomogeneities in exoplanets through transmission spectroscopy. Our approach links chromatic variations in conventional transit model parameters—central transit time, total and full durations, and transit depth—to atmospheric asymmetries. By separately analyzing atmospheric asymmetries during ingress and egress, we can derive clear connections between these variations and the underlying asymmetries of the planetary limbs. Additionally, this approach enables us to investigate differences between the limbs slightly offset from the terminator on the dayside and the nightside. We applied this method to JWST’s NIRSpec/G395H observations of the hot Saturn exoplanet WASP-39 b. Our analysis suggests a higher abundance of CO₂ on the evening limb compared to the morning limb and indicates a greater probability of SO₂ on the limb slightly offset from the terminator on the dayside relative to the nightside. These findings highlight the potential of our method to enhance the understanding of photochemical processes in exoplanetary atmospheres.

Keywords: Exoplanet atmospheres (487), Exoplanets (498), Transits (1711), Transmission spectroscopy (2133)

1. INTRODUCTION

The unprecedentedly precise transmission spectra obtained by the James Webb Space Telescope (JWST) have significantly advanced the study of close-in exoplanet atmospheres (e.g., Rustamkulov et al. 2023). For instance, the detection of SO₂ in the atmosphere of the hot Saturn WASP-39 b marked the first unambiguous identification of a photochemically produced molecule in an exoplanetary atmosphere (Alderson et al. 2023; Pow-

ell et al. 2024; Tsai et al. 2023b), showcasing JWST’s capability to probe photochemical processes. Simulations using a 3D Global Circulation Model (GCM) and a two-dimensional photochemical model have further suggested that SO₂ may accumulate on the planet’s nightside (Tsai et al. 2023a). While ultraviolet radiation from the host star drives photochemical reactions on the dayside, these reactions, coupled with atmospheric circulation, affect the global distribution of chemical species. These findings highlight the importance of studying atmospheric inhomogeneities to understand the interplay

between photochemical processes and atmospheric circulation.

Studies on atmospheric inhomogeneities are progressing rapidly. Recently, [Rustamkulov et al. \(2023\)](#) discovered that the central transit time of WASP-39 b observed with JWST’s NIRSpec/PRISM varies by seconds depending on the wavelength, suggesting potential morning-evening asymmetries in the planet’s limb. This finding aligns with predictions from studies using GCMs, which suggest that atmospheric asymmetries could cause the wavelength dependence of the central transit time ([Dobbs-Dixon et al. 2012](#)). Moreover, several studies using GCMs have investigated the effects of atmospheric inhomogeneities on transmission spectra (e.g., [Fortney et al. 2010](#); [Kempton et al. 2017](#)) and the shape of transit light curves (e.g., [Line & Parmentier 2016](#); [Falco et al. 2024](#)).

One approach to characterizing atmospheric asymmetries from such distortions in transit light curves is to analyze the data using a dedicated aspherical planet model ([von Paris et al. 2016](#); [Espinoza & Jones 2021](#); [Grant & Wakeford 2023](#)) instead of conventional transit modeling¹. The advantage of this approach is that it allows for the direct prediction of transit light curves from the asymmetrical model. [Espinoza et al. \(2024\)](#) applied one such model to the previously mentioned JWST data of WASP-39 b, deriving for the first time separate transmission spectra for the morning and evening limbs. Similarly, [Murphy et al. \(2024\)](#) used the same model to analyze JWST data of the warm Neptune WASP-107 b and derived separate transmission spectra for its morning and evening limbs.

However, these studies have predominantly focused on asymmetries in the morning-evening direction, ignoring potential asymmetries in the day-night or north-south directions. Day-night asymmetries, in particular, are closely linked to photochemical processes, making them critical for understanding photochemical processes on exoplanets. While high-resolution transmission spectroscopy has demonstrated the ability to separately investigate the atmospheric properties of the dayside and nightside of the terminator ([Gandhi et al. 2022](#)), it remains unclear how such day-night asymmetries can be effectively studied using low- to mid-resolution transmission spectroscopy. [Falco et al. \(2024\)](#) demonstrated that the effect of planetary rotation can modify the shape of transit light curves, as the slightly visible dayside or nightside influences the apparent radii of the limbs. This

finding suggests the potential to explore day-night asymmetries through detailed analyses of transit light curves.

In this paper, we explore atmospheric asymmetries beyond the morning-evening direction by linking the color dependence of conventional transit model parameters to atmospheric asymmetries on the planetary limbs. We analyze not only the color dependence of the central transit time but also the duration for the first time. By separately analyzing asymmetries during ingress and egress, we can derive clear connections between these chromatic variations and the underlying asymmetries of the planetary limbs. This approach also enables us to investigate differences between the limbs slightly offset from the terminator on the dayside and the nightside.

We refer to the variations in transit parameters with wavelength as chromatic transit variation (CTV) and aim to establish a general framework that links CTV to atmospheric asymmetries in planetary atmospheres. The structure of this paper is as follows: In §2, we formulate the relationship between CTV and atmospheric asymmetries. In §3, we validate the proposed method using synthetic data. In §4, we apply this method to JWST observations of WASP-39 b. §5 discusses the implications for planetary atmospheres, and §6 outlines future prospects.

2. IMPACT OF ATMOSPHERIC ASYMMETRY ON CONVENTIONAL TRANSIT MODELING

2.1. *How Does Atmospheric Asymmetry Affect Transit Parameters?*

In transmission spectroscopy, chromatic variations in the depth of the transit light curve are observed due to differences in the apparent radius of a planet at different wavelengths. These variations arise from the absorption and scattering of light by atmospheric molecules, clouds, and haze in the planet’s limb. Spatial asymmetries in the atmospheric structure of a planet’s limb, such as temperature and molecular abundance, also affect the transit light curve. How would these spatial asymmetries alter the parameters in the transit light curve?

Panel (a) of [Figure 1](#) shows the parameters of the transit light curve. The key characteristics of the light curve are described by five parameters: the transit depth k^2 and the four contact times, t_I , t_{II} , t_{III} , and t_{IV} . Here, k is the ratio of the planetary radius to the host star’s radius. These contact times can be converted into the timing of ingress $t_i = (t_I + t_{II})/2$, the duration of ingress $\tau_i = t_{II} - t_I$, the timing of egress $t_e = (t_{III} + t_{IV})/2$, and the duration of egress $\tau_e = t_{IV} - t_{III}$. For a circular orbit, there is a constraint $\tau_i = \tau_e$, leading to the useful conversions $t_0 = (t_I + t_{IV})/2 = (t_{II} + t_{III})/2$, $T_{\text{tot}} = t_{IV} - t_I$, and $T_{\text{full}} = t_{III} - t_{II}$. Here, t_0 is the central transit time,

¹ We refer to the transit model that assumes a circular planetary shadow and Keplerian motion as the conventional transit model.

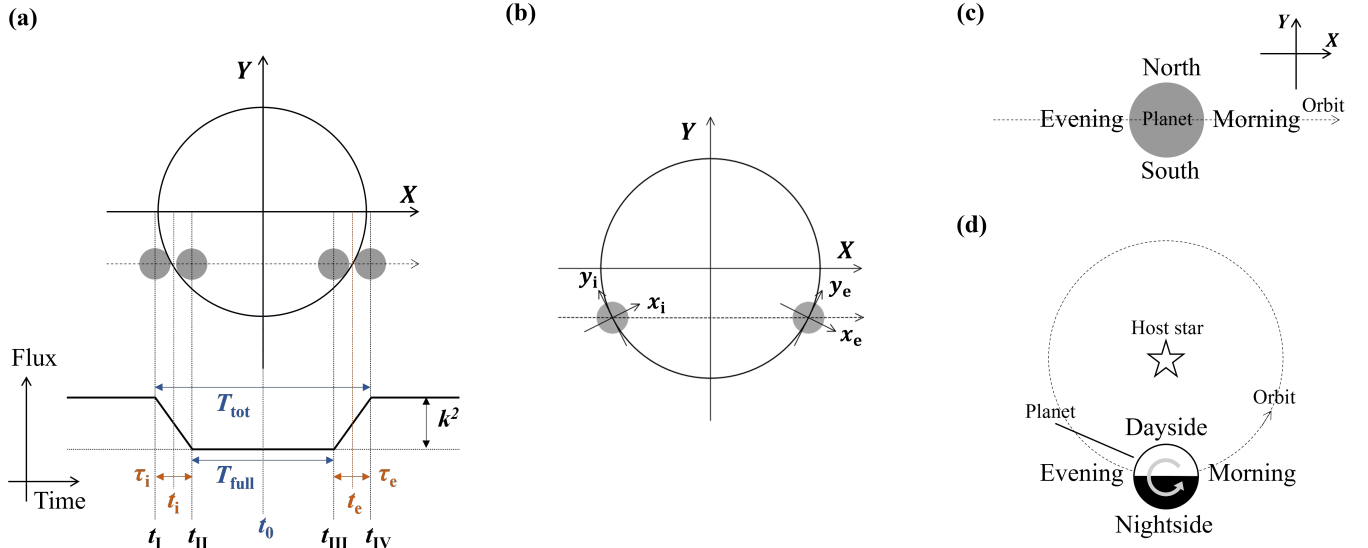


Figure 1. Definitions of parameters, coordinate systems, and directional terms used in this paper. (a) The definitions of parameters in the conventional transit model. k^2 represents the depth of the light curve. The four contact times, t_I , t_{II} , t_{III} , and t_{IV} , are defined as the times when the planet is externally and internally tangent to the stellar disk. These contact times can be converted as follows: $t_i = (t_I + t_{II})/2$, $\tau_i = t_{II} - t_I$, $t_e = (t_{III} + t_{IV})/2$, and $\tau_e = t_{IV} - t_{III}$. For a circular orbit, there is a constraint $\tau_i = \tau_e$, leading to the following useful conversions: $T_{\text{tot}} = t_{IV} - t_I$, $T_{\text{full}} = t_{III} - t_{II}$, and $t_0 = (t_I + t_{IV})/2 = (t_{II} + t_{III})/2$. (b) The coordinate systems used in this paper. The X - Y coordinate system is fixed relative to the celestial sphere. The y_i -axis and y_e -axis are aligned with the tangent lines of the stellar disk at the points where the planetary orbit intersects the edge of the host star. The x_i -axis and x_e -axis are oriented perpendicularly to the y_i -axis and y_e -axis, respectively. The x_i - y_i and x_e - y_e coordinate systems are fixed relative to the planet's center of mass and rotate synchronously with the planet's orbital motion, regardless of whether the planet itself is tidally locked. (c) The definitions of the north, south, morning, and evening. (d) The definitions of the morning, evening, dayside, and nightside. The planet's rotation is in the same direction as its orbital motion.

T_{tot} refers to the total duration during which any part of the planet is transiting, and T_{full} refers to the full duration during which the entire planet is transiting.

The coordinate systems used in this paper are shown in Panel (b) of Figure 1. The X - Y coordinate system follows Winn (2010). The host star is centered in this coordinate system. The dashed line represents the orbit of the planet's center of mass. To clarify the discussion, we also define the x_i - y_i and x_e - y_e coordinate systems. The y_i -axis and y_e -axis are aligned with the tangent lines of the stellar disk where the planet's orbit intersects the edge of the star, while the x_i -axis and x_e -axis are perpendicular to the y_i -axis and y_e -axis, respectively. The X - Y coordinate system is fixed relative to the celestial sphere, while the x_i - y_i and x_e - y_e coordinate systems are fixed relative to the planet's center of mass and rotate synchronously with the planet's orbital motion, regardless of whether the planet itself is tidally locked. This means that the x_i - y_i and x_e - y_e coordinate systems rotate in the same way as the planet's day-night terminator (see Figure 5).

In this paper, we assume that the planet's rotation is in the same direction as its orbital motion and refer to the planet's leading limb as the morning limb and

the trailing limb as the evening limb. This assumption includes the case of synchronous rotation due to tidal locking. Additionally, we define the positive Y direction as north, and the negative Y direction as south. Panel (c) and (d) of Figure 1 illustrate the definitions of these directional terms used in this paper.

In our model, atmospheric asymmetries are represented by slight displacements of the center of the planet's circular shadow disk from the center of mass. Figure 2 illustrates four different patterns of light curve changes. We can associate changes in the parameters of the conventional transit model with combinations of these patterns.

As shown in Panel (a) of Figure 2, a displacement of the planet's shadow toward the negative X direction at certain wavelengths (morning-evening asymmetry) causes an overall delay in the transit timing, shifting the central transit time, t_0 , to a later time (e.g. Dobbs-Dixon & Agol 2013; Espinoza et al. 2024). On the other hand, a displacement along the Y -axis (north-south asymmetry) affects the transit duration, as shown in Panel (b). The transit duration is also altered when the displacements along the X -axis are in opposite directions during ingress and egress (Panel (c)). This pat-

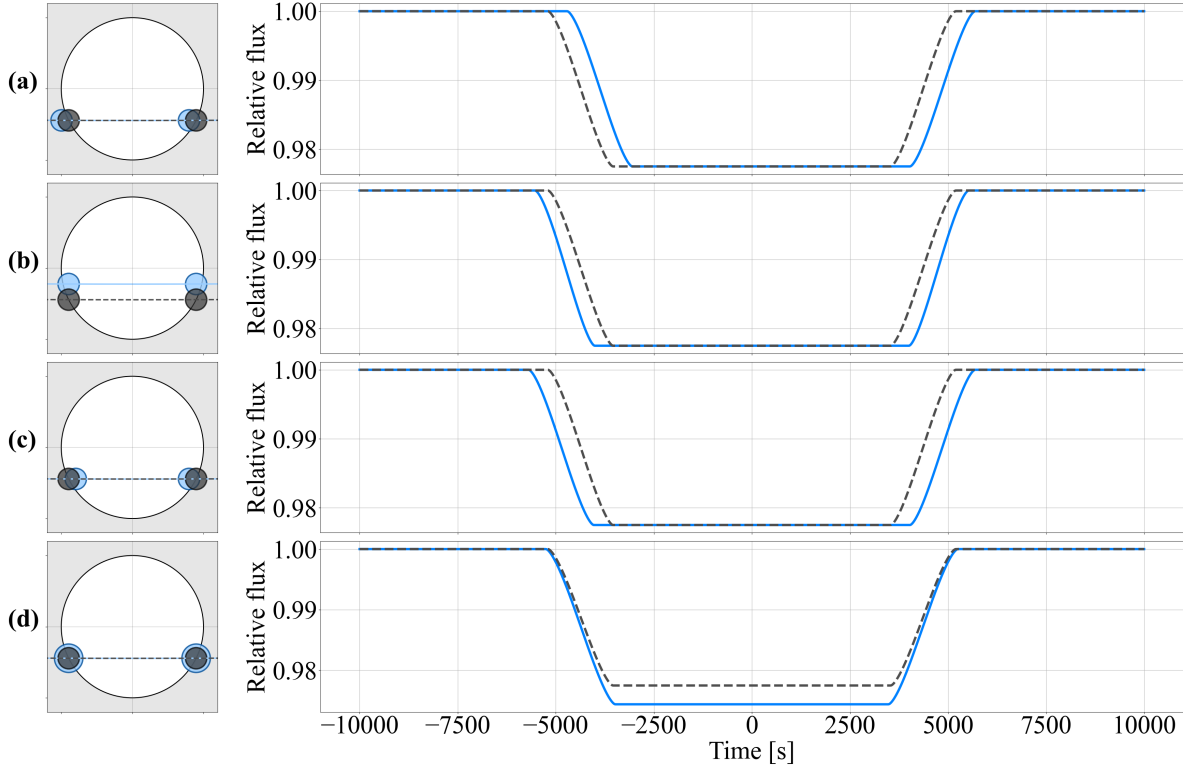


Figure 2. Patterns of atmospheric asymmetry and their different impacts on light curves. The blue solid lines and grey dashed lines in the figures on the right of each panel correspond to the light curves of the blue and grey disks of the planet’s shadow in the schematics on the left, respectively. (a) A displacement of the planet’s shadow along the X -axis (morning-evening asymmetry) causes a shift of the central transit time t_0 . (b) A displacement along the Y -axis (north-south asymmetry) causes a change in the transit duration. (c) Opposite displacements along the X -axis between ingress and egress also alter the transit duration. (d) Changes in the apparent radius result in variations in both the transit depth and duration. In Panel (d), the radius of the blue disk is exaggerated by a factor of 5 compared to the disk producing the blue light curve, to highlight the differences between the grey and blue disks.

tern reflects the difference in the light conditions of the limb between ingress and egress, which we further discuss in §2.2. Changes in the planet’s radius affect the transit depth k^2 and duration, without altering the central transit time, as shown in Panel (d).

To account for any asymmetries, it is necessary to introduce an additional pattern where the displacement of the planet’s shadow along the Y -axis differs between ingress and egress. However, this pattern is difficult to reconcile with the conventional transit model, as it results in different durations for ingress and egress, while the conventional model typically allows only slight differences between them (Winn 2010).

However, classifying asymmetries into four patterns in Figure 2, and considering their impact on the transit parameters, especially the durations T_{tot} and T_{full} , makes the analysis complex and difficult to interpret. To improve the clarity of the relationship between the light curve and asymmetries, we consider asymmetries in ingress and egress separately, focusing on the timing

of ingress t_i , the duration of ingress τ_i , the timing of egress t_e , and the duration of egress τ_e . Note that when assuming a circular orbit, there is a constraint of $\tau_i = \tau_e$, which we will discuss further in §2.4.

We find that τ_i remains constant with asymmetries in the direction of orbital motion, which is nearly aligned with the X direction, assuming the planet moves in uniform linear motion on the celestial sphere during ingress (Panel (a) of Figure 3). In contrast, asymmetries perpendicular to the orbital motion, which is nearly aligned with the Y direction, cause changes in τ_i .

On the other hand, t_i remains constant with asymmetries along the host star’s edge, which is nearly aligned with the y_i direction (Panel (b) of Figure 3). Strictly speaking, these asymmetries preserve the timing when the center of the planet’s shadow disk intersects the host star’s edge t'_i , which is slightly different from t_i (see Appendix A for details). Asymmetries perpendicular to the host star’s edge, which is nearly aligned with the x_i direction, cause changes in t'_i .

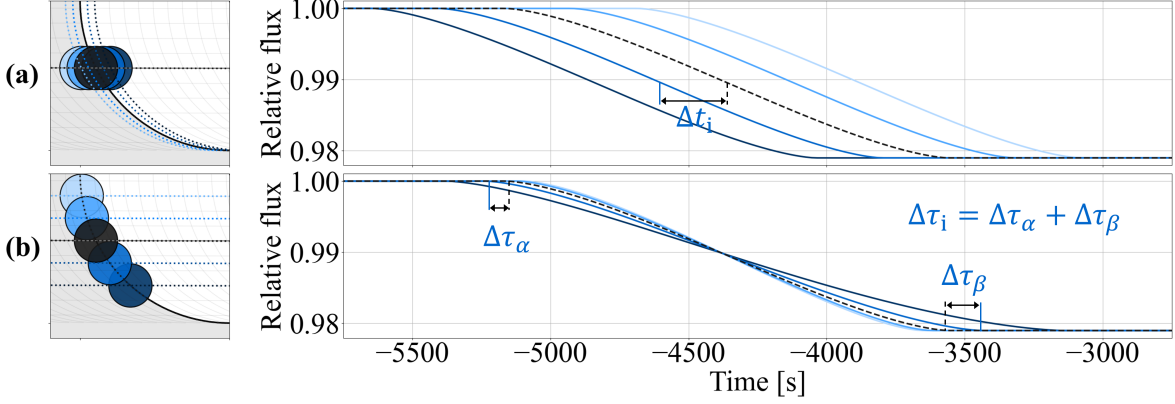


Figure 3. Changes in timing and duration of ingress caused by atmospheric asymmetries. The colored solid lines and grey dashed lines in the graphs on the right correspond to the light curves of the planet’s shadow disks with the same color in the schematics on the left, respectively. Thin grey lines in the schematics on the left show the lines of constant t'_i ($\sim t_i$) or τ_i . (a) Asymmetry in the direction of orbital motion preserves the duration of ingress τ_i . The colored dotted lines in the schematics on the left show the lines of constant t'_i for each planet’s shadow disk. (b) Asymmetry along the host star’s edge preserves the timing of ingress t'_i . The colored dotted lines in the schematics on the left show the lines of constant τ_i for each planet’s shadow disk.

Asymmetries in these directions do not strictly preserve the timing or duration because the projected velocity of the planet on the celestial sphere is not constant during ingress or egress. However, even considering this, the changes in those timings and durations are slight.

These patterns hold for egress as well: asymmetries in the direction perpendicular to the orbital motion, which is almost the same as the Y direction, cause changes in τ_e , while asymmetries in the direction perpendicular to the host star’s edge, which is almost the same as the x_e direction, cause changes in t_e .

We can determine the displacement vector of the center of the planet’s shadow disk from the center of mass for both ingress and egress separately. To first order, the x_i component of the vector is determined using t_i , and the Y component using τ_i for ingress. For egress, the x_e component is determined using t_e , and the Y component using τ_e .

We perform an order-of-magnitude estimation of the differences in the ingress timing Δt_i and duration $\Delta \tau_i$ from the reference. Δt_i arises from the difference in the apparent planetary radius in the direction perpendicular to the host star’s edge (the x_i direction), $\Delta R_p^{x_i} = R_p^{x_i+} - R_p^{x_i-}$. Here, $R_p^{x_i+}$ and $R_p^{x_i-}$ are the lengths of the projected planetary shadow onto the x_i -axis, measured from the planet’s center of mass in the positive x_i direction and negative x_i direction, respectively (Figure 4). Similarly, $\Delta \tau_i$ arises from the difference in the apparent planetary radius in the direction perpendicular to the orbital motion (the Y direction), $\Delta R_p^Y = R_p^{Y+} - R_p^{Y-}$. R_p^{Y+} and R_p^{Y-} are the length of the projected planetary

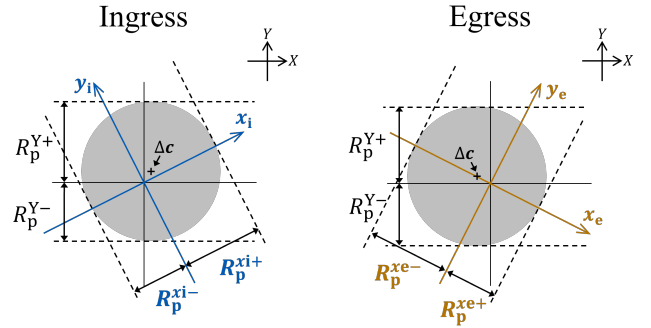


Figure 4. Definitions of $R_p^{x_i+}$, $R_p^{x_i-}$, $R_p^{x_e+}$, $R_p^{x_e-}$, R_p^{Y+} , and R_p^{Y-} . The origin of the x_i - y_i and x_e - y_e coordinate systems corresponds to the planet’s center of mass. Grey shadows represent the planet’s shadow at a certain wavelength, with two-dimensional displacement vectors Δc . R_p^{Y+} and R_p^{Y-} are the lengths of the projected planetary shadow onto the Y -axis, measured from the planet’s center of mass in the positive Y direction and negative Y direction, respectively. Similarly, $R_p^{x_i+}$ and $R_p^{x_i-}$ are the lengths of the projected planetary shadow onto the x_i -axis, measured from the planet’s center of mass in the positive x_i direction and negative x_i direction, respectively. The x_i - y_i plane corresponds to the X - Y plane at ingress (left). $R_p^{x_e+}$ and $R_p^{x_e-}$ are the lengths of the projected planetary shadow onto the x_e -axis, measured from the planet’s center of mass in the positive and negative x_e direction, respectively. The x_e - y_e plane corresponds to the X - Y plane at egress (right).

shadow onto the Y -axis, measured from the planet’s center of mass in the positive Y direction and negative Y direction, respectively (Figure 4). Δt_i and $\Delta \tau_i$ are

approximated as

$$\Delta t_i \sim -\frac{\Delta R_p^{xi}}{2v\sqrt{1-b^2}}, \quad (1)$$

$$\Delta \tau_i \sim \frac{\Delta R_p^Y}{2v} \left(\frac{b}{\sqrt{(1+k)^2 - b^2}} - \frac{b}{\sqrt{(1-k)^2 - b^2}} \right). \quad (2)$$

Here, $v \sim 2\pi a/P$ is the velocity of planetary orbital motion, where a is the semi-major axis and P is the orbital period. k^2 represents the depth of the light curve, and b is the impact parameter. $\Delta \tau_i$ can be derived by differentiating $\tau_i \sim R_s/v \left(\sqrt{(1+k)^2 - b^2} - \sqrt{(1-k)^2 - b^2} \right)$ with respect to b and using the conversion $\Delta b = -\Delta R_p^Y/(2R_s)$.

Assuming WASP-39 b with $P = 4$ days, $a = 11.4 R_s$, $k = 0.145$, $b = 0.45$, $R_s = 0.9 R_\odot = 6.3 \times 10^8$ m (Faedi et al. 2011), and $\Delta R_p^{xi}, \Delta R_p^Y = 1000$ km (\sim scale height), we obtain $\Delta t_i \sim -4$ s and $\Delta \tau_i \sim -0.7$ s. This magnitude of differences is measurable given the precision of JWST.

From these estimates, we find that the uncertainty in the atmospheric asymmetries in the Y direction is greater than that in the x_i direction. For WASP-39 b, the uncertainty of ΔR_p^Y is approximately $4 \div 0.7 \times 2 \sim 10$ times greater than that of ΔR_p^{xi} , considering the factor of 2 in the conversions $t_i = (t_I + t_{II})/2$ and $\tau_i = t_{II} - t_I$. Similar considerations apply to egress. Therefore, for both ingress and egress, the direction in which asymmetries can be measured with the highest precision is perpendicular to the host star's edges (the x_i and x_e directions). This motivated our use of the x_i - y_i and x_e - y_e coordinate systems in the formulation in §2.3. In the case where $b \sim 0$, $\Delta \tau_i$ is nearly zero, meaning that almost no information can be obtained about asymmetries along the Y axis.

2.2. Light Conditions of Limb During Transit

Displacements of the planet's shadow along the Y -axis can arise not only from north-south asymmetries in the planet's day-night terminator itself but also from the effect of an orbital inclination that is not exactly 90 degrees, which allows a slight view of the dayside (Figure 5). Therefore, displacements along the Y -axis can also be interpreted as differences between the limbs slightly offset from the terminator on the dayside versus the nightside. This creates different light conditions between the north and south limbs. These differences in light conditions could cause variations in photochemical processes, resulting in different atmospheric properties.

As shown in Figure 5, the direction in which the dayside is visible changes between ingress and egress.

This direction corresponds to the positive x_i direction at ingress and the negative x_e direction at egress.

The difference in the light conditions of the atmosphere at two opposing limbs observable during transit is most pronounced along the x_i -axis at ingress and the x_e -axis at egress. Figure 6 illustrates the differences in light conditions between these limbs. At the limbs in the positive x_i direction and the negative x_e direction, light primarily passes through the atmosphere slightly offset from the terminator on the dayside. In contrast, at the limbs in the negative x_i direction and the positive x_e direction, light primarily passes through the atmosphere slightly offset from the terminator on the nightside. The angle between the terminator plane and the x_i axis at ingress or the x_e axis at egress is given by $\arcsin(R_s/a)$, where R_s is the host star's radius and a is the semi-major axis.

2.3. Formulation

Next, we formulate this approach and derive the relationship between asymmetries and the following parameters: the contact times $t_I, t_{II}, t_{III}, t_{IV}$, and the transit depth k^2 . In our model, atmospheric asymmetries are represented by the slight displacement of the center of the planet's shadow disk from the center of mass. The shadow disk has a specific radius at each wavelength. This modeling allows the use of conventional transit model light curve fitting for each wavelength. Therefore, the asymmetry at wavelength λ is expressed by a two-dimensional displacement vector $\Delta \mathbf{c}(\lambda)$ and its radius $R_p(\lambda)$. We aim to obtain $\Delta \mathbf{c}(\lambda)$ as a function of $t_I(\lambda), t_{II}(\lambda)$, and $k(\lambda)$ at ingress, and $t_{III}(\lambda), t_{IV}(\lambda)$, and $k(\lambda)$ at egress. Since we use the planet's center of mass as a reference for displacement, the assumption about the orbit of the planet's center of mass is important. We will discuss this point further in §2.5. In this section, we assume the orbit of the planet's center of mass is known.

The coordinate system of our formulation is shown in Panel (b) of Figure 1. The length is normalized by the stellar radius at a reference wavelength λ_0 . In our formulation, we take the wavelength dependence of the stellar radius $R_s(\lambda)$ into account, by using the ratio of the stellar radii at wavelength λ and λ_0 ,

$$\alpha(\lambda) = \frac{R_s(\lambda)}{R_s(\lambda_0)}. \quad (3)$$

The observed planetary radius $R_p(\lambda)$ divided by $R_s(\lambda_0)$ is expressed as

$$\frac{R_p(\lambda)}{R_s(\lambda_0)} = \alpha(\lambda)k(\lambda), \quad (4)$$

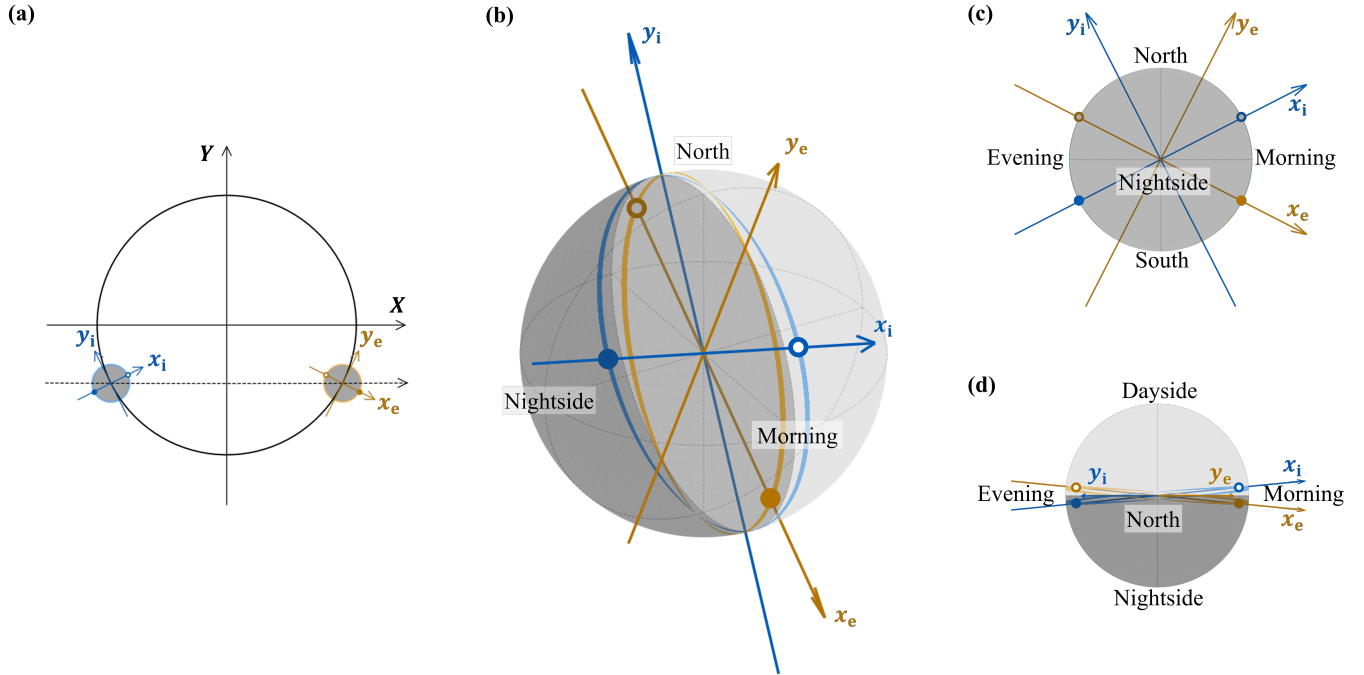


Figure 5. Positions of limbs observable during ingress and egress on the planet, as expected from the orbital parameters of WASP-39 b. Panel (a) is similar to Panel (b) of Figure 1, but the x_i -axis and y_i -axis are colored blue, and the x_e -axis and y_e -axis are colored orange. The blue and orange points indicate where the limbs intersect the x_i -axis or x_e -axis. The white-filled points represent those on the dayside of the northern hemisphere, while the filled points represent those on the nightside of the southern hemisphere. The limb observable during ingress is colored blue and the limb observable during egress is colored orange. Panels (b), (c), and (d) show the positions of the x_i -axis, y_i -axis (blue), x_e -axis, and y_e -axis (orange), and the limbs observable during ingress (blue belt) and egress (orange belt) on the planet. The finite width of each belt reflects the shift caused by the planet's rotation during ingress or egress. The white and gray hemispheres represent the dayside and nightside of the planet, respectively. Panel (c) shows the view from the nightside, and Panel (d) shows the view from the north. The limbs observable during ingress and egress are shifted slightly away from the terminator. The y_i -axis and y_e -axis intersect the terminator.

where $k(\lambda) = R_p(\lambda)/R_s(\lambda)$.

First, let's consider the case of ingress. Since $t_I(\lambda)$ and $t_{II}(\lambda)$ are defined as the times when the planet is externally tangent to and internally tangent to the stellar disk, respectively, we obtain

$$|\mathbf{c}(\lambda, t_I(\lambda))| = \alpha(\lambda)(1 + k(\lambda)) \quad (5)$$

$$|\mathbf{c}(\lambda, t_{II}(\lambda))| = \alpha(\lambda)(1 - k(\lambda)), \quad (6)$$

where $\mathbf{c}(\lambda, t)$ indicates the trajectory of the center of the planet's shadow disk at wavelength λ in the X - Y coordinate system.

Assuming that the atmospheric asymmetries at the planetary limb do not change during ingress, $\mathbf{c}(\lambda, t)$ is expressed as

$$\mathbf{c}(\lambda, t) = \mathbf{c}_b(t) + \Delta\mathbf{c}(\lambda), \quad (7)$$

where $\mathbf{c}_b(t)$ is the trajectory of the center of mass of the planet. The change of planetary phase during ingress is ignored on this assumption, however, this is reasonable because the duration of ingress is much shorter than the

orbital period of planets. We define

$$\mathbf{m}(\lambda; t_I(\lambda), t_{II}(\lambda)) = \frac{\mathbf{c}_b(t_I(\lambda)) + \mathbf{c}_b(t_{II}(\lambda))}{2} \quad (8)$$

$$\mathbf{d}(\lambda; t_I(\lambda), t_{II}(\lambda)) = \frac{\mathbf{c}_b(t_I(\lambda)) - \mathbf{c}_b(t_{II}(\lambda))}{2}. \quad (9)$$

Here, \mathbf{m} represents the midpoint between the coordinates of the planet's center of mass at t_I and t_{II} , and \mathbf{d} represents half of the displacement between the coordinates of the planet's center of mass at t_I and t_{II} . If we assume that planets move in uniform linear motion during ingress, $\mathbf{m}(\lambda; t_I(\lambda), t_{II}(\lambda))$ is proportional to $t_i = (t_I + t_{II})/2$, and $\mathbf{d}(\lambda; t_I(\lambda), t_{II}(\lambda))$ is proportional to $\tau_i = t_{II} - t_I$.

Using equations (5), (6) and (7), we obtain the simultaneous equations,

$$\begin{cases} |\mathbf{m} + \mathbf{d} + \Delta\mathbf{c}| = \alpha(1 + k) \\ |\mathbf{m} - \mathbf{d} + \Delta\mathbf{c}| = \alpha(1 - k), \end{cases} \quad (10)$$

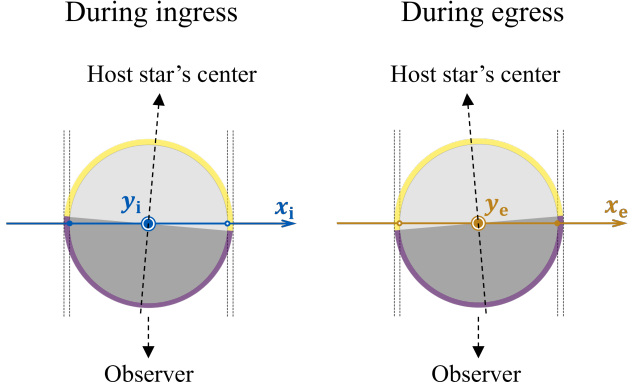


Figure 6. Light conditions of the atmosphere transmitted by the host star's light during ingress (left) and egress (right), as expected from the orbital parameters of WASP-39 b. The y_i -axis (for ingress) and y_e -axis (for egress) are normal to the plane of the paper and directed out of the page. The white and gray semicircles represent the planet's dayside and nightside, respectively. The yellow and purple regions represent the atmosphere of the dayside and nightside, respectively. The blue and orange points indicate where the limbs observed during ingress or egress intersect the x_i -axis or x_e -axis. White-filled points represent positions in the positive x_i or negative x_e directions, while filled points represent those in the negative x_i or positive x_e directions. Dashed arrows show the direction toward the center of the host star and the observer, which are not aligned. Therefore, the light conditions of the atmosphere at the positive x_i limb versus the negative x_i limb, or at the positive x_e limb versus the negative x_e limb are different. The atmosphere between the dashed lines on each limb contributes to the transmission spectrum.

where the arguments are omitted for readability. We convert these equations into

$$\begin{cases} \mathbf{d} \cdot (\mathbf{m} + \Delta\mathbf{c}) = \alpha^2 k \\ |\mathbf{m} + \Delta\mathbf{c}|^2 = \alpha^2(1 + k^2) - |\mathbf{d}|^2. \end{cases} \quad (11)$$

Defining a rotation matrix by

$$\mathcal{R}_d = \frac{1}{|\mathbf{d}|} \begin{pmatrix} d_X & -d_Y \\ d_Y & d_X \end{pmatrix}, \quad (12)$$

where $(d_X, d_Y)^\top = \mathbf{d}$, we obtain the following expression from equation (11)

$$\mathcal{R}_d^\top (\mathbf{m} + \Delta\mathbf{c}) = \mathbf{s} \quad (13)$$

where

$$\begin{aligned} \mathbf{s} &= \left(\alpha^2 \frac{k}{|\mathbf{d}|}, \pm \sqrt{\alpha^2(1 + k^2) - |\mathbf{d}|^2} - \left(\alpha^2 \frac{k}{|\mathbf{d}|} \right)^2 \right)^\top \\ &= \alpha \left(\frac{\alpha k}{|\mathbf{d}|}, \pm \sqrt{\left(1 - \frac{|\mathbf{d}|^2}{\alpha^2}\right) \left(1 - \frac{\alpha^2 k^2}{|\mathbf{d}|^2}\right)} \right)^\top. \end{aligned} \quad (14)$$

When the inclination of the orbit is not 90° , we can choose smaller $\Delta\mathbf{c}$ by adopting the positive sign in equation (14). However, if the inclination is almost 90° , it is difficult to determine which sign is correct. In such cases, we cannot determine the direction of atmospheric asymmetries along the Y -axis.

By solving equation (13) for $\Delta\mathbf{c}$, we finally obtain

$$\Delta\mathbf{c} = -\mathbf{m} + \mathcal{R}_d \mathbf{s}. \quad (15)$$

The vector \mathbf{m} represents the midpoint of the planet's center of mass at t_I and t_{II} , while $\mathcal{R}_d \mathbf{s}$ represents the midpoint of the center of the planet's shadow disk at wavelength λ at t_I and t_{II} . \mathbf{m} is primarily determined by t_i , while $\mathcal{R}_d \mathbf{s}$ is primarily determined by τ_i .

The displacement for egress can also be determined by defining $\mathbf{m}(\lambda)$ and $\mathbf{d}(\lambda)$ as

$$\mathbf{m}(\lambda; t_{III}(\lambda), t_{IV}(\lambda)) = \frac{\mathbf{c}_b(t_{IV}(\lambda)) + \mathbf{c}_b(t_{III}(\lambda))}{2} \quad (16)$$

$$\mathbf{d}(\lambda; t_{III}(\lambda), t_{IV}(\lambda)) = \frac{\mathbf{c}_b(t_{IV}(\lambda)) - \mathbf{c}_b(t_{III}(\lambda))}{2}, \quad (17)$$

and solving simultaneous equations (10). For egress, we have to adopt the negative sign in \mathbf{s} (equation (14)) to choose smaller $\Delta\mathbf{c}$.

We can convert the displacement vector $\Delta\mathbf{c}$ into the length from the planet's center of mass to the edge of the planetary shadow in the direction of the vector $\mathbf{e}_\theta = (\cos \theta, \sin \theta)^\top$, denoted as $R_p^\theta(\lambda)/R_s(\lambda_0)$. Here, θ is the angle measured counterclockwise from the X -axis. From the relationship

$$\left| \frac{R_p^\theta(\lambda)}{R_s(\lambda_0)} \mathbf{e}_\theta - \Delta\mathbf{c}(\lambda) \right| = \alpha(\lambda)k(\lambda), \quad (18)$$

we obtain

$$\frac{R_p^\theta(\lambda)}{R_s(\lambda_0)} = \mathbf{e}_\theta \cdot \Delta\mathbf{c} + \sqrt{\alpha^2 k^2 - |\Delta\mathbf{c}|^2 + (\mathbf{e}_\theta \cdot \Delta\mathbf{c})^2}, \quad (19)$$

where the arguments are omitted for readability.

However, as mentioned in §2.1, the sensitivity of the light curve shape to the magnitude of displacement along the Y direction is much lower than that along the x_i direction (about 10 times lower for the WASP-39 b case). The current data quality is insufficient to determine the Y component accurately. This applies to egress as well. Therefore, in this paper, we focus on the information obtained from the x_i component of $\Delta\mathbf{c}$ during ingress and the x_e component of $\Delta\mathbf{c}$ during egress.

For ingress, to transform the X - Y coordinate system into the x_i - y_i coordinate system, we define the following rotation matrix as

$$\mathcal{R}_i = \begin{pmatrix} c_{b,X}(t_{ib}) & -c_{b,Y}(t_{ib}) \\ c_{b,Y}(t_{ib}) & c_{b,X}(t_{ib}) \end{pmatrix}, \quad (20)$$

where $\mathbf{c}_b(t) = (c_{b,X}(t), c_{b,Y}(t))^T$, t_{ib} is the time when the planet's center of mass intersects the edge of the host star during ingress. The displacement vector in the x_i - y_i coordinate system is then given by

$$\Delta \mathbf{c}_i = -\mathcal{R}_i^T \Delta \mathbf{c}. \quad (21)$$

Similarly, for egress, the displacement vector in the x_e - y_e coordinate system is written as

$$\Delta \mathbf{c}_e = \mathcal{R}_e^T \Delta \mathbf{c}, \quad (22)$$

where

$$\mathcal{R}_e = \begin{pmatrix} c_{b,X}(t_{eb}) & -c_{b,Y}(t_{eb}) \\ c_{b,Y}(t_{eb}) & c_{b,X}(t_{eb}) \end{pmatrix} \quad (23)$$

is the rotation matrix for the egress case, and t_{eb} is the time when the planet's center of mass intersects the edge of the host star during egress.

For ingress, the x_i component of the displacement can be converted into the lengths R_p^{xi+} and R_p^{xi-} as shown in Figure 4. Similarly, for egress, the x_e component of the displacement can be converted into the lengths R_p^{xe+} and R_p^{xe-} . Note that R_p^{xi+} , R_p^{xi-} , R_p^{xe+} , and R_p^{xe-} are not exact radii, but projected lengths of the planet's shadow disk onto the x_i -axis or x_e -axis, measured from the planet's center of mass. The conversions are given by

$$\begin{aligned} \frac{R_p^{xi+}(\lambda)}{R_s(\lambda_0)} &= \alpha(\lambda)k(\lambda) + \Delta c_{i,x_i}(\lambda; t_I(\lambda), t_{II}(\lambda), k(\lambda)) \\ \frac{R_p^{xi-}(\lambda)}{R_s(\lambda_0)} &= \alpha(\lambda)k(\lambda) - \Delta c_{i,x_i}(\lambda; t_I(\lambda), t_{II}(\lambda), k(\lambda)) \\ \frac{R_p^{xe+}(\lambda)}{R_s(\lambda_0)} &= \alpha(\lambda)k(\lambda) + \Delta c_{e,x_e}(\lambda; t_{III}(\lambda), t_{IV}(\lambda), k(\lambda)) \\ \frac{R_p^{xe-}(\lambda)}{R_s(\lambda_0)} &= \alpha(\lambda)k(\lambda) - \Delta c_{e,x_e}(\lambda; t_{III}(\lambda), t_{IV}(\lambda), k(\lambda)), \end{aligned} \quad (24)$$

where $\Delta c_{i,x_i}(\lambda)$ is the x_i component of $\Delta \mathbf{c}_i(\lambda)$, and $\Delta c_{e,x_e}(\lambda)$ is the x_e component of $\Delta \mathbf{c}_e(\lambda)$. This means that we can derive the spectra of R_p^{xi+} and R_p^{xi-} from the chromatic variations in the parameters t_I , t_{II} , and k^2 , and the spectra of R_p^{xe+} and R_p^{xe-} from the chromatic variations in the parameters t_{III} , t_{IV} , and k^2 .

2.4. Constraints Imposed by Using the Conventional Transit Model

We use the conventional transit model to infer t_I , t_{II} , t_{III} , t_{IV} , and k^2 from observed data. However, it introduces certain constraints. Ideally, we would like to treat ingress and egress independently in the above formulation. This means that the parameters for ingress t_I , t_{II} , and k_i^2 , and the parameters for egress t_{III} , t_{IV} , and k_e^2 ,

should be independent. Here, k_i^2 and k_e^2 represent the transit depths for ingress and egress, respectively. However, the conventional transit model imposes the constraint $k_i^2 = k_e^2 = k^2$, which means the apparent planetary radius is assumed to be the same for both ingress and egress at each wavelength. If the difference between k_i^2 and k_e^2 becomes significant enough to pose a problem, the light curve depths during ingress and egress would differ. In such cases, verifying that the shape of the light curve remains sufficiently symmetric could serve as a way to assess whether this assumption is valid.

Additionally, the four contact times are not treated independently. If we assume a circular orbit, it imposes the constraint $\tau_i = \tau_e$, meaning that the durations of ingress and egress are the same. In this case, the four contact times can be expressed by three parameters, T_{tot} , T_{full} , and t_0 (Panel (a) of Figure 1), as follows:

$$\begin{aligned} t_I &= t_0 - \frac{T_{tot}}{2} \\ t_{II} &= t_0 - \frac{T_{full}}{2} \\ t_{III} &= t_0 + \frac{T_{full}}{2} \\ t_{IV} &= t_0 + \frac{T_{tot}}{2}. \end{aligned} \quad (25)$$

Even when considering a non-zero orbital eccentricity, the difference between τ_i and τ_e remains small (Winn 2010). Since τ_i and τ_e reflect the Y component of $\Delta \mathbf{c}(\lambda)$, the condition $\tau_i = \tau_e$ imposes the constraint that the Y component of $\Delta \mathbf{c}(\lambda)$ must be the same for both ingress and egress at each wavelength. However, given the sensitivity of τ_i and τ_e to the magnitude of displacement and the current data quality, the impact of this constraint is likely not significant.

A more flexible model than the conventional transit model is required to remove these constraints. Exploring such models is beyond the scope of this paper.

2.5. Impact of the Planet's Center of Mass Orbit on the Spectra

Since we use the planet's center of mass as a reference for the displacement of the planet's shadow disk, accurately determining the orbital parameters of the planet's center of mass is crucial for investigating atmospheric asymmetries from transit light curves, as highlighted by Espinoza et al. (2024). While the orbital parameters determined from transit data at wavelengths that exhibit small radii are considered to be close to those of the center of mass (Dobbs-Dixon et al. 2012), these parameters cannot be accurately determined solely from transit light curves because they are affected by atmospheric asymmetries. Although the values measured using the radial

velocity method are reliable, achieving the precision required for our analysis is not feasible with current observational capabilities. Therefore, it is essential to discuss how variations in these orbital parameters could impact the inferred spectra.

For simplicity, we assume a circular orbit with zero eccentricity. A detailed analysis considering the effects of orbital eccentricity is presented in §3. Under this assumption, the trajectory of the planet's center of mass $\mathbf{c}_b(t)$ can be expressed as

$$\mathbf{c}_b(t) = \begin{pmatrix} a \sin\left(2\pi \frac{t-t_{0b}}{P}\right) \\ -b \cos\left(2\pi \frac{t-t_{0b}}{P}\right) \end{pmatrix}, \quad (26)$$

where P is the orbital period, a is the semi-major axis, b is the impact parameter, and t_{0b} is the central transit time of the center of mass.

For ingress, $\mathbf{m}(\lambda)$ can be approximated as follows

$$\begin{aligned} \mathbf{m}(\lambda) &= \frac{\mathbf{c}_b(t_I(\lambda)) + \mathbf{c}_b(t_{II}(\lambda))}{2} \\ &= \begin{pmatrix} a \sin\left(2\pi \frac{t_i(\lambda)-t_{0b}}{P}\right) \cos\left(\pi \frac{\tau_i(\lambda)}{P}\right) \\ -b \cos\left(2\pi \frac{t_i(\lambda)-t_{0b}}{P}\right) \cos\left(\pi \frac{\tau_i(\lambda)}{P}\right) \end{pmatrix} \\ &\approx \begin{pmatrix} 2\pi a \frac{t_i(\lambda)-t_{0b}}{P} \\ -b \left(1 - \frac{1}{2} \left(2\pi \frac{t_i(\lambda)-t_{0b}}{P}\right)^2 - \frac{1}{2} \left(\pi \frac{\tau_i(\lambda)}{P}\right)^2\right) \end{pmatrix}, \end{aligned} \quad (27)$$

where $2\pi(t_i(\lambda) - t_{0b})/P \ll 1$ and $\pi\tau_i(\lambda)/P \ll 1$ were used, retaining second-order terms in the approximation. Interpreting \mathbf{m} as a function of the orbital parameters a , b , and t_{0b} , and considering small changes Δa , Δb , and Δt_{0b} , we have

$$\begin{aligned} \Delta \mathbf{m} &= \frac{\partial \mathbf{m}}{\partial a} \Delta a + \frac{\partial \mathbf{m}}{\partial b} \Delta b + \frac{\partial \mathbf{m}}{\partial t_{0b}} \Delta t_{0b} \\ &\approx \begin{pmatrix} 2\pi \left(\frac{t_i(\lambda)-t_{0b}}{P} \Delta a - \frac{a}{P} \Delta t_{0b}\right) \\ -\Delta b + 2\pi b \frac{t_i(\lambda)-t_{0b}}{P} \Delta t_{0b} \end{pmatrix}, \end{aligned} \quad (28)$$

This indicates that variations in \mathbf{m} are largely wavelength-independent, as the wavelength dependence of $(t_i(\lambda) - t_{0b})/P$ is minimal compared to that of $\Delta \mathbf{c}(\lambda)$. Given that the term $\mathcal{R}_d \mathbf{s}$ in equation (15) is determined by \mathbf{d} and is approximately positioned on the host star's edge, variations in \mathbf{d} have a negligible impact on the x_i component of $\Delta \mathbf{c}(\lambda)$, and consequently on the $R_p^{x_i+}$ and $R_p^{x_i-}$ spectra. Therefore, changes in a , b , and t_{0b} primarily result in offsets in the x_i component of $\Delta \mathbf{c}(\lambda)$, affecting the offsets but not the shape of the $R_p^{x_i+}$ and $R_p^{x_i-}$ spectra. The same applies to the spectra from egress, $R_p^{x_e+}$ and $R_p^{x_e-}$.

If the x_i component of $\Delta \mathbf{m}$ increases, the offset of the $R_p^{x_i+}$ spectra decreases, while the offset of the $R_p^{x_i-}$

spectra increases. Similarly, if the x_e component of $\Delta \mathbf{m}$ increases, the offset of the $R_p^{x_e+}$ spectra decreases, while that of the $R_p^{x_e-}$ spectra increases. As a result, negative values of Δa , Δb , or Δt_{0b} decrease the offset of the $R_p^{x_i+}$ spectra and increase the offset of the $R_p^{x_i-}$ spectra at ingress. Positive values of Δa or Δb , or negative values of Δt_{0b} decrease the offset of the $R_p^{x_e+}$ spectra and increase the offset of the $R_p^{x_e-}$ spectra at egress. Therefore, inaccuracies in a or b affect north-south asymmetries, while inaccuracies in t_{0b} affect morning-evening asymmetries.

Thus, even if the estimated orbital parameters of the planet's center of mass are inaccurate, the shape of the $R_p^{x_i+}$, $R_p^{x_i-}$, $R_p^{x_e+}$, and $R_p^{x_e-}$ spectra remains largely unaffected. However, careful consideration is required when interpreting inferred values, such as the VMRs of molecules or temperature, as spectral offsets can influence these results.

2.6. Wavelength Dependence of Host Star's Radius

In the formulation, the wavelength dependence of the host star's radius, denoted as $\alpha(\lambda)$, is taken into account. Simulations based on a stellar atmospheric model suggest a wavelength-dependent variation in stellar radii (Appendix B). The wavelength dependence of apparent stellar radii has not been well studied observationally, especially in the near-infrared region. While observations of giant stars, such as Mira variables, suggest a general increase in radius with wavelength in the near-infrared (e.g., Millan-Gabet et al. 2005; Witkowski et al. 2008), similar measurements have not been conducted for main-sequence stars, including the Sun, within this wavelength range (Rozelet et al. 2016).

However, transit duration provides valuable information. We can express $R_s(\lambda)$ as

$$R_s(\lambda) = a \sqrt{\sin^2\left(\frac{\pi T_{bc}(\lambda)}{P}\right) + \cos^2\left(\frac{\pi T_{bc}(\lambda)}{P}\right) \cos^2 i}, \quad (29)$$

where a is the semi-major axis, i is the inclination, and $T_{bc}(\lambda)$ is the transit duration for the center of mass of the planet. However, due to atmospheric asymmetries, the exact values of $T_{bc}(\lambda)$ are not directly measurable, making it challenging to disentangle the wavelength dependence of $T_{bc}(\lambda)$ from transit data alone. For simplicity, in §4, we use $(T_{tot} + T_{full})/2$ as a proxy for $T_{bc}(\lambda)$ (see Appendix A) and assume that the linear trend of $(T_{tot} + T_{full})/2$ can be attributed to $\alpha(\lambda)$.

Given these difficulties, it is essential to evaluate how inaccuracies in $\alpha(\lambda)$ may affect the inferred spectra of $R_p^{x_i+}$, $R_p^{x_i-}$, $R_p^{x_e+}$, and $R_p^{x_e-}$. Inaccuracies in $\alpha(\lambda)$ primarily influence the inferred spectra through their impact on \mathbf{s} , as defined in equation (14). When $\alpha(\lambda) > 1$,

the length of \mathbf{s} increases, leading to a smaller x_i component or a larger x_e component of $\Delta\mathbf{c}$ compared to the case where $\alpha(\lambda) = 1$. As a result, R_p^{xi+} and R_p^{xe-} decrease, while R_p^{xi-} and R_p^{xe+} increase compared to the case where $\alpha(\lambda) = 1$. Similarly, when $\alpha(\lambda) < 1$, R_p^{xi+} and R_p^{xe-} increase, while R_p^{xi-} and R_p^{xe+} decrease compared to the case where $\alpha(\lambda) = 1$. Notably, the effect of $\alpha(\lambda)$ is opposite between the spectra of the north and south limbs. These changes in the spectra of R_p^{xi+} , R_p^{xi-} , R_p^{xe+} , and R_p^{xe-} can affect the inferred volume mixing ratios of molecules and atmospheric temperatures during atmospheric retrievals. Therefore, careful consideration is required when interpreting these inferred values.

Although this does not apply to WASP-39, which we investigate in §4, a potential method for constraining the wavelength dependence of the host star’s radius is to observe the transit durations of planets with negligible atmospheric asymmetries, such as those with thin atmospheres. For example, transits of Mercury and Venus have been used to estimate the solar radius (Emilio et al. 2012, 2015).

3. VALIDATION OF THE METHOD

This section validates the method by recovering atmospheric asymmetry signals from simulated transit light curves. Additionally, we examine potential false signals of asymmetry introduced by the method. For simplicity, $\alpha = R_s(\lambda)/R_s(\lambda_0)$ is set to 1 in the following simulations, assuming no wavelength dependence of the stellar radius. While the effect of α was discussed in §2.6, we revisit this effect in §3.3. The simulations presented here utilized the Python packages `jaxoplanet` (Hattori et al. 2024) and `karate` (<https://github.com/sh-tada/karate>). The `karate` package provides functions for converting the planetary radius and contact times into $\Delta\mathbf{c}$ during ingress and egress, or R_p^{xi+} , R_p^{xi-} , R_p^{xe+} , and R_p^{xe-} .

3.1. Recovering Morning-Evening Asymmetries

First, we examine whether the wavelength-dependent morning-evening asymmetries of the planetary shadow can be accurately recovered from simulated transit light curves. Light curves were simulated using `catwoman` (Jones & Espinoza 2020; Espinoza & Jones 2021), which models the planetary shadow as two semi-circles with independently adjustable radii to represent atmospheric asymmetries between the morning and evening terminators. In this simulation, we set φ , the angle between the direction of the planet’s orbital motion and the boundary of the semi-circles (Figure 7), to 90° to model a morning-evening asymmetry.

We focused on a planet with zero eccentricity. The remaining orbital parameters were based on WASP-39

Table 1. Parameters and prior distributions for the transit light curve model under the assumption of a circular orbit, used in the MCMC analysis of simulated light curves.

Symbol	Description	Prior
k^2	transit depth	$\mathcal{U}(0, 0.1)$
t_0	central transit time [s]	$\mathcal{U}(-5000, 5000)$
T_{tot}	total transit duration [s]	$\mathcal{U}(5000, 15000)$
T_{full}	full transit duration [s]	$\mathcal{U}(1, T_{\text{full}}^{\text{max}})$
c_{base}	baseline coefficient	$\mathcal{U}(0.99, 1.01)$
<i>jitter</i>	jitter error	$\mathcal{U}(0, 0.01)$
u_1	limb darkening coefficient	$\mathcal{U}(-3, 3)$
u_2	limb darkening coefficient	$\mathcal{U}(-3, 3)$

NOTE— $\mathcal{U}(a, b)$: the uniform distribution from a to b . $T_{\text{full}}^{\text{max}}$ is defined in equation (33).

b, with an orbital period $P = 4.06$ days, semi-major axis $a = 11.4 R_s$, and impact parameter $b = 0.45$ (Faedi et al. 2011). The time of inferior conjunction t_0 was set to 0, and the coefficients of a quadratic limb-darkening model (u_1, u_2) were set to (0.1, 0.1).

The radius of the morning-side semi-circle, $R_p^{\text{morning}}(\lambda)$, and the radius of the evening-side semi-circle, $R_p^{\text{evening}}(\lambda)$ (Figure 7), varied from 0.145 to $0.155 R_s$ independently, generating 21 normalized transit light curves. For ease of visualization, these light curves were assigned wavelengths ranging from 3 to $5 \mu\text{m}$. The integration time was set to 65 seconds, closely matching the 63.14 seconds used in observational data for WASP-39 b obtained with JWST NIRSpec/G395H (Alderson et al. 2023; Stevenson et al. 2016; Bean et al. 2018), analyzed in §4. Both noiseless data and data with added Gaussian noise (mean = 0, standard deviation = 250 ppm) were generated to simulate observational uncertainties. The noise level, with a standard deviation of 250 ppm, is comparable to the most precise light curves analyzed in §4.

First, we measured the planetary radius k and contact times t_I , t_{II} , t_{III} , and t_{IV} from the simulated light curves using the conventional transit light curve model assuming a circular orbit. The analysis employed the Hamiltonian Monte Carlo - No U-Turn Sampler (HMC-NUTS), a specific Markov Chain Monte Carlo (MCMC) algorithm, implemented in NumPyro (Phan et al. 2019). The parameters of the transit light curve model and their prior distributions are summarized in Table 1. The light curve baseline was assumed to be constant (c_{base}). The likelihood of the light curve data was modeled as a normal distribution, with the mean defined as the product of the transit light curve model and the baseline,

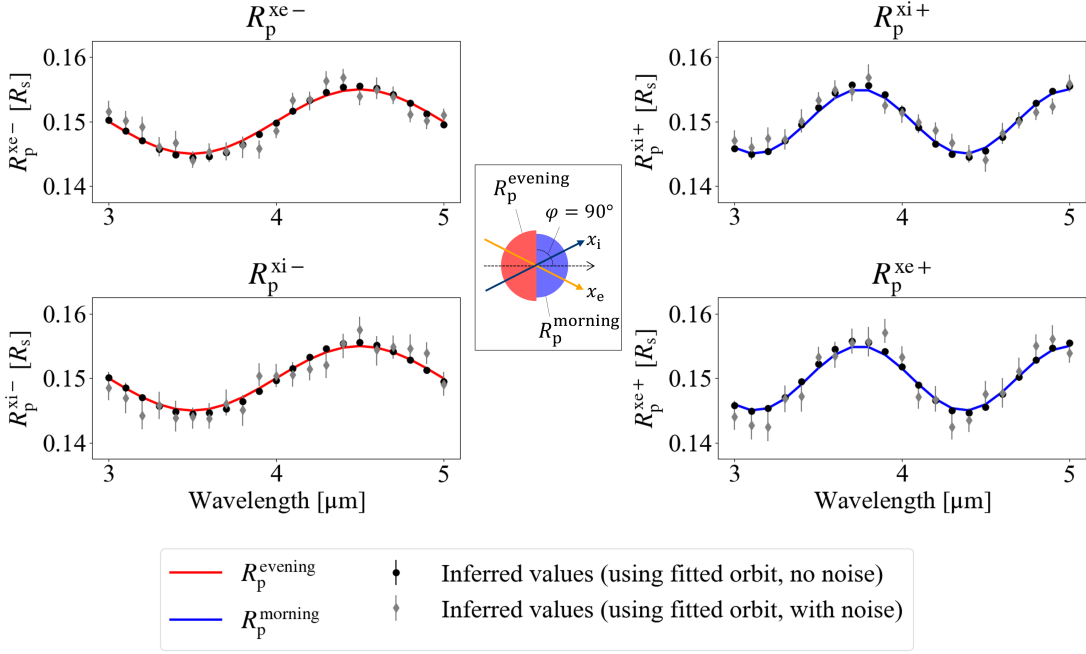


Figure 7. Inferred values of R_p^{xi+} , R_p^{xi-} , R_p^{xe+} , and R_p^{xe-} based on the MCMC analysis of light curves simulated using *catwoman* (Jones & Espinoza 2020; Espinoza & Jones 2021). The values were converted using the estimated orbital parameters. The dots represent the median values from the MCMC sampling, while the error bars indicate the 68% credible intervals. Results are shown for both noiseless data and data with added Gaussian noise (mean = 0, standard deviation = 250 ppm). The true values of R_p^{morning} (blue) and R_p^{evening} (red) are shown as colored lines. The arrangement of the panels reflects the positional relationship between the regions on the planet contributing to each spectrum, as viewed from the night side. The central panel shows the shape of the planetary shadow, along with the x_i -axis, x_e -axis. φ is the angle between the direction of the planet's orbital motion and the boundary of the semi-circles, set to 90° to model a morning-evening asymmetry. The radius of the morning-side semi-circle is denoted as R_p^{morning} , and the radius of the evening-side semi-circle is denoted as R_p^{evening} .

and the variance modeled as *jitter*². In this analysis, the orbital period P was fixed to its true value.

The semi-major axis a and inclination i were derived from the transit depth k^2 , the central transit time t_0 , the total transit duration T_{tot} , and the full transit duration T_{full} as follows

$$a = \sqrt{\frac{(1+k)^2 \cos^2\left(\frac{\pi T_{\text{full}}}{P}\right) - (1-k)^2 \cos^2\left(\frac{\pi T_{\text{tot}}}{P}\right)}{\sin\left(\frac{\pi T_{\text{tot}} + \pi T_{\text{full}}}{P}\right) \sin\left(\frac{\pi T_{\text{tot}} - \pi T_{\text{full}}}{P}\right)}} \quad (30)$$

$$\cos i = \sqrt{\frac{-(1+k)^2 \sin^2\left(\frac{\pi T_{\text{full}}}{P}\right) + (1-k)^2 \sin^2\left(\frac{\pi T_{\text{tot}}}{P}\right)}{(1+k)^2 \cos^2\left(\frac{\pi T_{\text{full}}}{P}\right) - (1-k)^2 \cos^2\left(\frac{\pi T_{\text{tot}}}{P}\right)}} \quad (31)$$

Valid values for a and i can only be obtained if k^2 , T_{tot} , and T_{full} satisfy the following condition

$$\begin{cases} (1-k)^2 \sin^2\left(\frac{\pi T_{\text{tot}}}{P}\right) - (1+k)^2 \sin^2\left(\frac{\pi T_{\text{full}}}{P}\right) \geq 0 \\ T_{\text{tot}} > T_{\text{full}}. \end{cases} \quad (32)$$

To avoid indeterminate solutions, we impose an upper bound on T_{full} , which is defined by

$$T_{\text{full}}^{\text{max}} = \frac{P}{\pi} \arcsin\left(\frac{1-k}{1+k} \sin\left(\frac{\pi T_{\text{tot}}}{P}\right)\right). \quad (33)$$

The inferred values of k , t_I , t_{II} , t_{III} , and t_{IV} can be converted to Δc during ingress and egress by assuming the orbital parameters of the planet's center of mass. Here, we derive these orbital parameters from the inferred values obtained through the MCMC analysis. We calculate the median of the MCMC samples converted into orbital parameters of a , b , and t_0 for each light curve, and then take the mean of these medians as the orbital parameters for the conversion. For noiseless data and data with added Gaussian noise, the resulting orbital parameters were $(a, b, t_0) = (11.404 R_s, 0.449, 0.783 \text{ s})$ and $(11.409 R_s, 0.449, 2.86 \text{ s})$, respectively. These values deviate from the true values due to the asymmetries in the planetary shadow, even in the case of noiseless data. The orbital period P used for the conversion was the true value.

We can convert k , $\Delta c_{e,xe}$, and $\Delta c_{i,xi}$ to R_p^{xi+} , R_p^{xi-} , R_p^{xe+} , and R_p^{xe-} using equation (24). The resulting spectra are shown in Figure 7. Based on the shape of the

planetary shadow, R_p^{xi+} and R_p^{xe+} are expected to reflect the spectrum of $R_p^{morning}$, while R_p^{xi-} and R_p^{xe-} are expected to reflect the spectrum of $R_p^{evening}$. The inferred values align closely with these expectations. These results demonstrate that this method can effectively capture morning-evening asymmetries, even when the shape of the planetary shadow deviates from being perfectly circular.

3.2. Symmetric Planets with Non-Zero Eccentricity

Next, we confirm that no asymmetries are detected from the transit light curves of symmetric planets. To assess the impact of planetary eccentricity on asymmetry detection, we analyzed simulated transit light curves for three planets with different eccentricities e and arguments of periastron ω . The three cases considered are $(e \cos \omega, e \sin \omega) = (0, 0)$, $(0.1, 0)$, and $(0, 0.1)$. We simulated normalized transit light curves by varying k , the ratio of the planetary radius to the stellar radius, from 1.45 to 1.55, generating 21 light curves for each planet. All other parameters for the light curve simulation were identical to those described in §3.1. Both noiseless data and data with added Gaussian noise (mean = 0, standard deviation = 250 ppm) were generated to simulate observational uncertainties. The analysis procedures were identical to those described in §3.1. It should be noted that the transit light curves of planets with elliptical orbits were also fitted using the circular orbit model.

The simulated noiseless light curves of symmetric planets with elliptical orbits, $(e \cos \omega, e \sin \omega) = (0.1, 0)$ and $(0, 0.1)$, along with fitted light curves using the circular orbit model, are shown in Figure 8. The residuals are small, indicating that light curves with non-zero eccentricity can be well-fitted using the circular orbit model.

Figure 9 shows the inferred values of $k = R_p/R_s$ and the contact times t_I , t_{II} , t_{III} , and t_{IV} for the three planets, along with their true values. Results are presented for both noiseless data and data with added Gaussian noise. The inferred values closely match the true values. This result reflects the fact that the difference in the durations of ingress and egress is approximately $e \cos \omega (R_s/a)^3$, which remains small even for planets with non-zero eccentricity (Winn 2010). Focusing on the noiseless data, the errors in k were nearly zero. For the planet with $e = 0$, the errors in the contact times were also nearly zero. For planets with $(e \cos \omega, e \sin \omega) = (0.1, 0)$ and $(0, 0.1)$, the errors in the contact times were ~ 0.1 s. These results indicate that, for these planets, as long as the uncertainty of the inferred values exceeds approximately 0.1 s, using

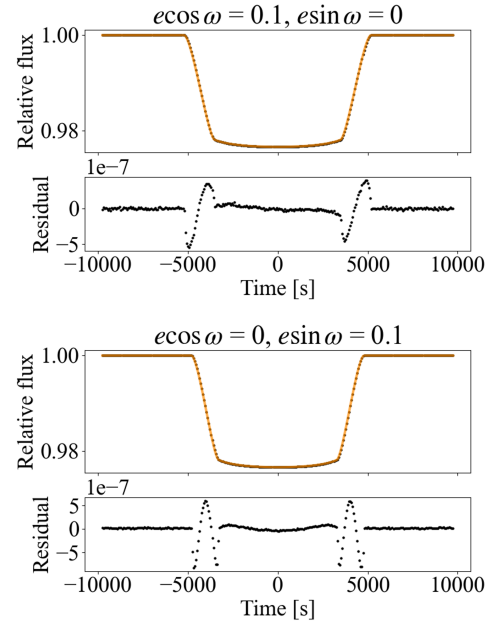


Figure 8. Simulated noiseless light curves of symmetric planets with elliptical orbits (black dots) and fitted light curves using the circular orbit model (orange lines). The bottom panels show the residuals. (Top) Case of $(e \cos \omega, e \sin \omega) = (0.1, 0)$. (Bottom) Case of $(e \cos \omega, e \sin \omega) = (0, 0.1)$.

a circular orbit model to measure these values does not introduce significant errors.

The inferred values of k , t_I , t_{II} , t_{III} , and t_{IV} can be converted to $\Delta \mathbf{c}$ during ingress and egress by assuming the orbital parameters of the planet’s center of mass. The orbital parameters used for these conversions were $(a, b, t_0) = (11.400 R_s, 0.4500, -5.7 \times 10^{-5} \text{ s})$, $(11.457 R_s, 0.4455, -8.653 \text{ s})$, and $(12.593 R_s, 0.4056, -3.6 \times 10^{-5} \text{ s})$ for planets with $(e \cos \omega, e \sin \omega) = (0, 0)$, $(0.1, 0)$, and $(0, 0.1)$, respectively.

Figure 10 presents the converted Δc_X and Δc_Y during ingress and egress, focusing on the noiseless data. For comparison, Δc_X and Δc_Y converted using the true orbital parameters are also shown. The results indicate that $\Delta \mathbf{c}$ values converted using the estimated orbital parameters closely match the true value of zero, with errors less than $1 \times 10^{-4} R_s$. Despite the presence of errors ~ 0.1 s in the measured contact times for planets with $(e \cos \omega, e \sin \omega) = (0.1, 0)$ and $(0, 0.1)$, the orbital parameters estimated from the MCMC analysis effectively represent an averaged position of the planetary shadow during ingress and egress. Consequently, $\Delta \mathbf{c}$, the relative position of the planetary shadow, can be measured accurately. In contrast, $\Delta \mathbf{c}$ values converted

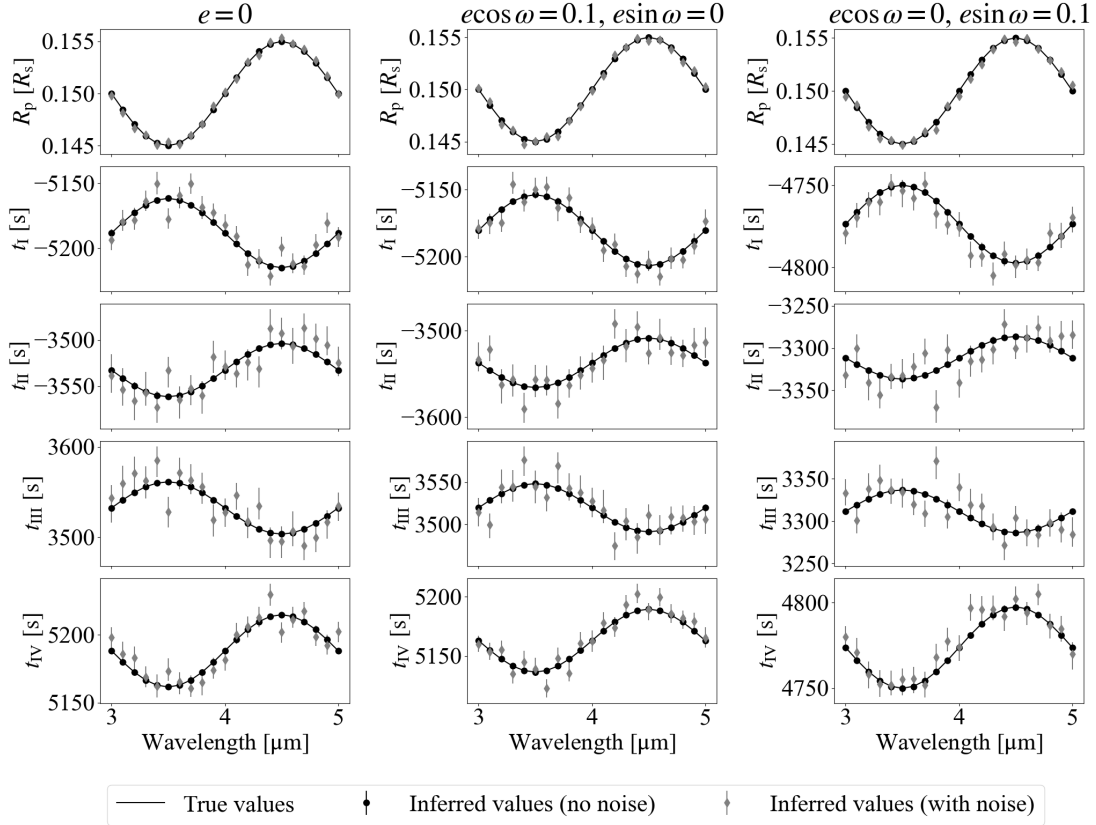


Figure 9. Inferred values of $k = R_p/R_s$ and the contact times t_I , t_{II} , t_{III} , and t_{IV} for three symmetric planets with $(e \cos \omega, e \sin \omega) = (0, 0)$, $(0.1, 0)$, and $(0, 0.1)$, based on the MCMC analysis of simulated data. The circular orbit model was used to derive these values in the MCMC analysis. The dots represent the median values from the MCMC sampling, while the error bars indicate the 68% credible intervals. Results are shown for both noiseless data and data with added Gaussian noise (mean = 0, standard deviation = 250 ppm), along with the true values.

using the true orbital parameters show small shifts from zero, reflecting the errors in the measured contact times.

Figure 11 shows the inferred values of R_p^{xi+} , R_p^{xi-} , R_p^{ee+} , and R_p^{ee-} . For both noiseless data and data with added Gaussian noise, the estimated orbital parameters were used for these conversions. The results demonstrate that the inferred values closely match the true values and do not detect any false asymmetries.

3.3. Asymmetric Planet with Day-Night Asymmetries

Here, we examine whether the wavelength-dependent displacement of the planetary shadow can be accurately recovered from simulated transit light curves. In the light curve simulation, the X and Y components of the displacement $\Delta \mathbf{c}$ varied with wavelength, ranging from -0.005 to $0.005 R_s$, respectively. These variations were defined independently for ingress and egress. Since Δc_X and Δc_Y take different values for ingress and egress, they exhibit time dependence. In this simulation, Δc_X and Δc_Y were constant before t_{II} and after t_{III} , and varied linearly with time between t_{II} and t_{III} . All other parameters for the light curve simulation were identical to

those described in §3.2. For this analysis, we focused on a planet with zero eccentricity because, as confirmed in §3.2, the effect of planetary eccentricity is negligible, at least for $e < 0.1$. Both noiseless data and data with added Gaussian noise (mean = 0, standard deviation = 250 ppm) were generated to simulate observational uncertainties. The analysis procedures were identical to those described in §3.1.

Figure 12 shows the inferred values of selected parameters for the planet with the displacement $\Delta \mathbf{c}$, along with their true values and the corresponding values for a symmetric planet. The results include $k = R_p/R_s$, the timing of ingress t_i , the timing of egress t_e , the duration of ingress τ_i , and the duration of egress τ_e , as these parameters are closely related to atmospheric asymmetries, as described in §2. Results are presented for both noiseless data and data with added Gaussian noise. The inferred values closely match the true values. In the panel for τ_i and τ_e , the true values of both τ_i and τ_e are plotted but are difficult to distinguish, as the lines are very close and nearly overlap. This highlights the low sensitivity of τ_i and τ_e to atmospheric asymmetries, as described

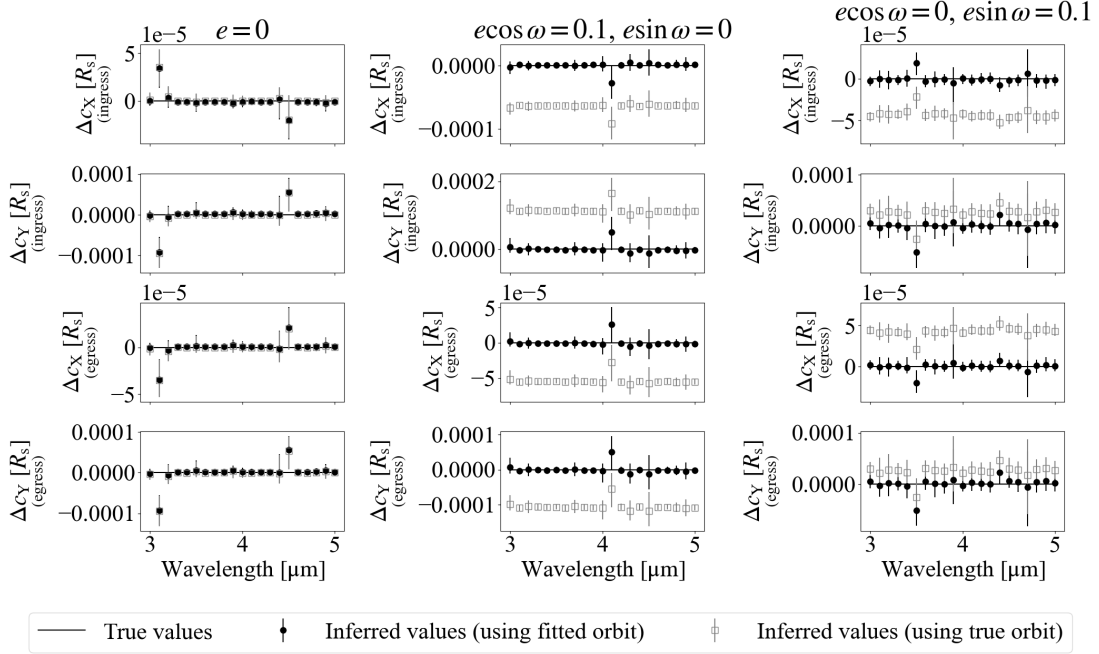


Figure 10. Inferred values of Δc_X and Δc_Y during ingress and egress for three symmetric planets with $(e \cos \omega, e \sin \omega) = (0, 0)$, $(0.1, 0)$, and $(0, 0.1)$, based on the MCMC analysis of simulated data. The values converted using both estimated and true orbital parameters are shown. The circular orbit model was used to derive these values in the MCMC analysis. The dots represent the median values from the MCMC sampling, and the error bars indicate the 68% credible intervals. Results are shown only for noiseless data, along with the true values.

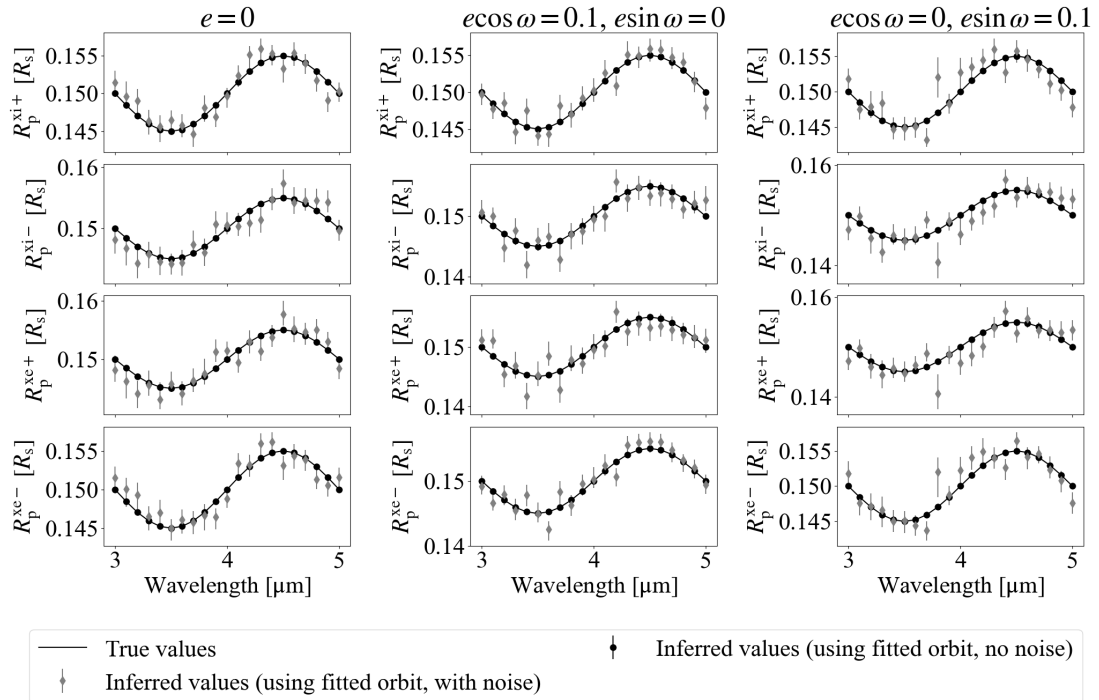


Figure 11. Inferred values of R_p^{xi+} , R_p^{xi-} , R_p^{xe+} , and R_p^{xe-} for three symmetric planets with $(e \cos \omega, e \sin \omega) = (0, 0)$, $(0.1, 0)$, and $(0, 0.1)$, based on the MCMC analysis of simulated data. The values were converted using the estimated orbital parameters. The circular orbit model was used in the MCMC analysis to derive these values. The dots represent the median values from the MCMC sampling, while the error bars indicate the 68% credible intervals. Results are shown for both noiseless data and data with added Gaussian noise (mean = 0, standard deviation = 250 ppm), along with the true values.

in §2, implying the challenges of measuring atmospheric asymmetry along the Y-axis.

We derived the orbital parameters from the inferred values obtained through the MCMC analysis and con-

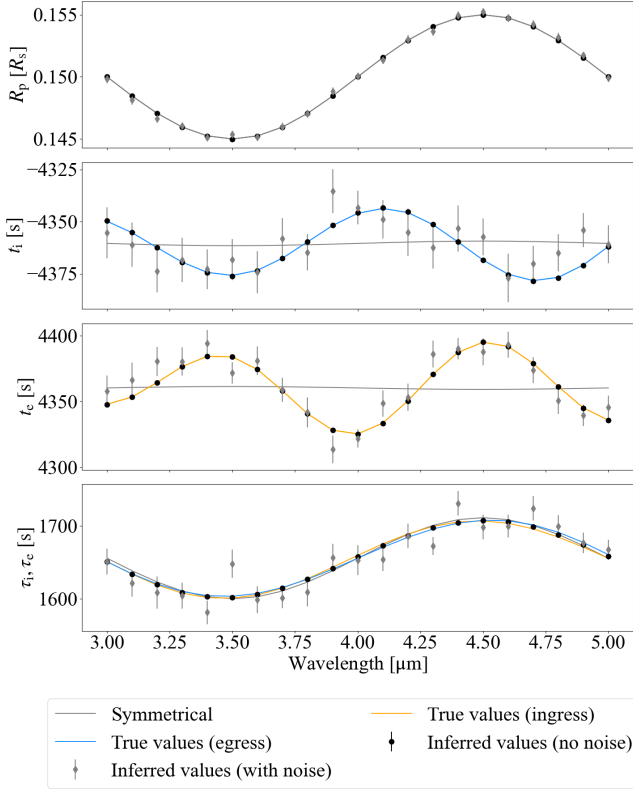


Figure 12. Inferred values of $k = R_p/R_s$, the timing of ingress t_i , the timing of egress t_e , the duration of ingress τ_i , and the duration of egress τ_e for an asymmetric planet, based on the MCMC analysis of simulated data. The dots represent the median values from the MCMC sampling, while the error bars indicate the 68% credible intervals. Results are shown for both noiseless data and data with added Gaussian noise (mean = 0, standard deviation = 250 ppm), along with the true values (colored lines). The values for a symmetric planet are also plotted (gray lines). The inferred τ_i and τ_e are identical because a circular orbit model was used in the analysis. In the panel for τ_i and τ_e , the true values of both are plotted but are difficult to distinguish as the lines are very close and nearly overlap.

verted k , t_I , t_{II} , t_{III} , and t_{IV} to $\Delta\mathbf{c}$. The orbital parameters used for these conversions were $(a, b, t_0) = (11.399 R_s, 0.4494, -0.663 \text{ s})$ for noiseless data, and $(a, b, t_0) = (11.403 R_s, 0.4488, 1.426 \text{ s})$ for data with added Gaussian noise.

Figure 13 shows the converted values of $\Delta c_{i,xi}$, $\Delta c_{e,xe}$, and Δc_Y during ingress and egress. For comparison, the values converted using the true orbital parameters are also shown for noiseless data. The converted $\Delta c_{i,xi}$ and $\Delta c_{e,xe}$ closely align with the true values. However, for noiseless data, the values converted using the estimated orbital parameters exhibit slight shifts compared to the true values or those derived using the true orbital parameters. This discrepancy arises because the

orbital parameters estimated from the MCMC analysis are influenced by atmospheric asymmetries, leading to offset-like errors in the converted values.

The inferred values of Δc_Y do not accurately reproduce the true values. This is because the inferred Δc_Y values for ingress and egress are nearly identical, as discussed in §2.4. Instead, these values are comparable to the mean of the true Δc_Y at ingress and egress. Nevertheless, for data with added noise, the large uncertainties associated with Δc_Y effectively mask this limitation, making it negligible in practice.

In §2.5, we investigated the effect of errors in the orbital parameters of the planet’s center of mass. We found that these errors have an almost wavelength-independent effect on $\Delta c_{i,xi}$ and $\Delta c_{e,xe}$, or R_p^{xi+} , R_p^{xi-} , R_p^{xe+} , and R_p^{xe-} . This can be confirmed by examining the partial derivatives of these values with respect to each orbital parameter. Since the `karate` package is built on JAX (Bradbury et al. 2018), a library for array-oriented numerical computation with automatic differentiation, we can efficiently compute the partial derivatives of these values.

For simplicity, the functions used to estimate the partial derivatives were $\Delta c_{i,xi}$ and $\Delta c_{e,xe}$, which were derived by converting the median values of k , t_I , t_{II} , t_{III} , and t_{IV} obtained from the MCMC analysis using the orbital parameters estimated from the same analysis, $(a, b, t_0) = (11.399 R_s, 0.4494, -0.663 \text{ s})$. These functions were treated as functions of the orbital parameters including the orbital period P , $e \cos \omega$, and $e \sin \omega$, and the wavelength dependence of the host star’s radius α , for the calculation of partial derivatives. Here, e denotes the eccentricity, and ω is the argument of periastron.

Figure 14 shows the partial derivatives of $\Delta c_{i,xi}$ and $\Delta c_{e,xe}$ with respect to each parameter. These derivatives were evaluated at the values estimated from the MCMC analysis along with other parameters: $P = 4.06 \text{ days}$, $e = 10^{-10}$, $\omega = 0$, and $\alpha = 1$. For the evaluation of partial derivatives with respect to $e \cos \omega$ and $e \sin \omega$, a small non-zero value was assigned to e . The results indicate that all partial derivatives are nearly wavelength-independent. As described in §2.5 and 2.6, inaccuracies in a , b , and $\alpha = R_s(\lambda)/R_s(\lambda_0)$ primarily affect north-south asymmetries, while inaccuracies in t_0 primarily affect morning-evening asymmetries. This interpretation aligns with the opposite signs of the partial derivatives of $\Delta c_{i,xi}$ and $\Delta c_{e,xe}$ with respect to a and b , and the identical signs of those with respect to t_0 . Similarly, inaccuracies in P or $e \sin \omega$ affect north-south asymmetries, whereas inaccuracies in $e \cos \omega$ affect morning-evening asymmetries.

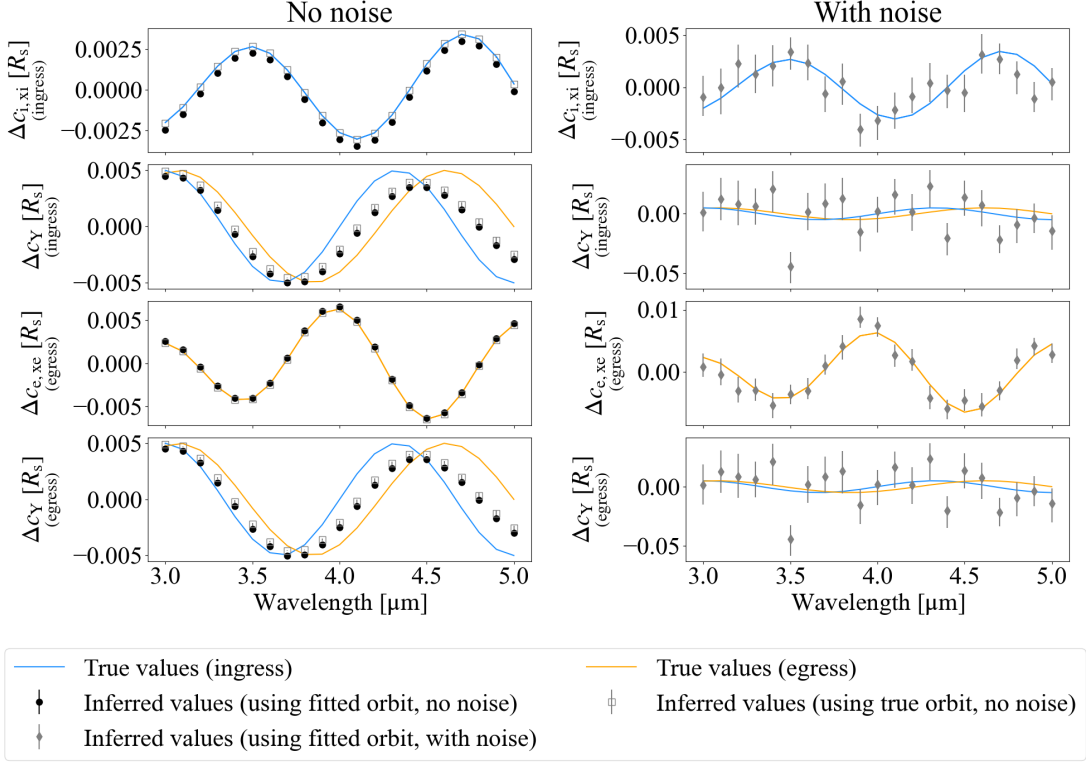


Figure 13. Inferred values of $\Delta c_{i,xi}$, $\Delta c_{e,xe}$, and Δc_Y during ingress and egress for an asymmetric planet, based on the MCMC analysis of simulated data. The values were converted using the estimated orbital parameters. The dots represent the median values from the MCMC sampling, and the error bars indicate the 68% credible intervals. Results are shown for noiseless data (left) and data with added Gaussian noise (mean = 0, standard deviation = 250 ppm) (right), along with the true values.

Table 2. Parameter errors corresponding to a $+0.001 R_s$ offset in $\Delta c_{i,xi}$ and $\Delta c_{e,xe}$.

Parameter	$\delta(\Delta c_{i,xi}) = 0.001$	$\delta(\Delta c_{e,xe}) = 0.001$
δP	-400 s	+400 s
δt_0	+5 s	+5 s
δa	+0.01 R_s	-0.01 R_s
δb	+0.002	-0.002
$\delta(e \cos \omega)$	-0.06	-0.06
$\delta(e \sin \omega)$	+0.002	-0.002
$\delta \alpha$	-0.001	+0.001

Using the partial derivatives, we can estimate the parameter errors required to produce a $+0.001 R_s$ offset in $\Delta c_{i,xi}$ and $\Delta c_{e,xe}$ (Table 2). Note that these values vary for planets with different orbital parameters.

We can convert k , $\Delta c_{i,xi}$, and $\Delta c_{e,xe}$ to R_p^{xi+} , R_p^{xi-} , R_p^{xe+} , and R_p^{xe-} using equation (24). The resulting spectra are shown in Figure 15. Results are presented for both noiseless data and data with added Gaussian noise. The inferred values closely align with the true values. These results demonstrate that, despite the limitations imposed by the conventional transit model, this method

can effectively capture atmospheric asymmetries in these directions.

4. APPLICATION TO JWST NIRSpec G395H DATA OF WASP-39 b

In this section, we apply the method described in the previous section to the hot Saturn, WASP-39 b, around a G8 host star, which has a mass of $\sim 0.28 M_{\text{Jup}}$, a radius of $\sim 1.27 R_{\text{Jup}}$, an equilibrium temperature of ~ 1100 K, and an orbital period of ~ 4.05 days (Faedi et al. 2011). As the Introduction mentions, WASP-39 b was the first to have its t_0 chromatic variation reported by Rustomkulov et al. (2023) using NIRSpec/PRISM observations. Furthermore, Espinoza et al. (2024) analyzed the morning-evening asymmetries using these data.

4.1. Data

We used the data taken with JWST NIRSpec/G395H (Jakobsen et al. 2022; Böker et al. 2023) on 2022 July 30–31, as part of the JWST Transiting Exoplanet Community Director’s Discretionary Early Release Science (JTEC ERS) Program (Alderson et al. 2023; Stevenson et al. 2016; Bean et al. 2018, ERS-1366). These data have the highest spectral resolution ($R \sim 3000$) among the data taken in the JTEC ERS Program, and

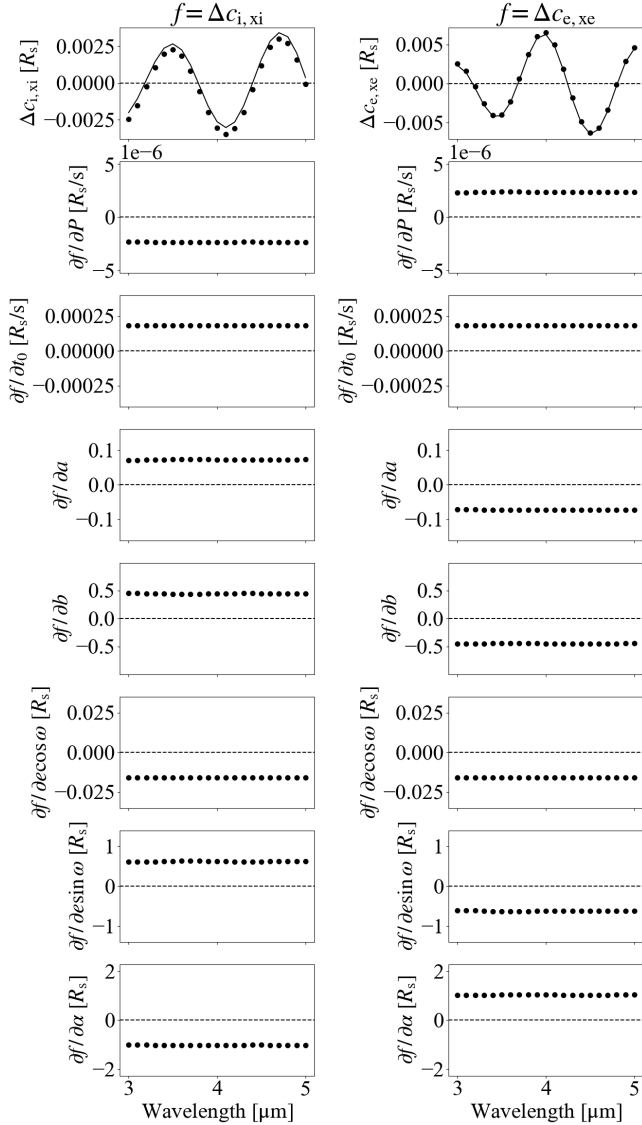


Figure 14. Partial derivatives of $\Delta c_{i,xi}$ (left) and $\Delta c_{e,xe}$ (right) with respect to each orbital parameter. The functions used to estimate the partial derivatives were $\Delta c_{i,xi}$ and $\Delta c_{e,xe}$, which were derived by converting the median values of k , t_I , t_{II} , t_{III} , and t_{IV} obtained from the MCMC analysis using the orbital parameters estimated from the same analysis. $\Delta c_{i,xi}$ and $\Delta c_{e,xe}$ are also shown at the top panels, along with the true values.

have higher precision than the other data with NIR-Spec/PRISM at the same spectral resolution (Sarkar et al. 2024). The wavelength range used in this analysis was 2.8–5.0 μm , which provides high-precision spectra.

To obtain the spectral time series, we performed data reduction using stages 1 and 2 of the ExoTiC-JEDI pipeline (Alderson et al. 2023). Stage 1 was almost the same as that of the JWST pipeline (Bushouse et al. 2024), with custom bias subtraction replacing the pipeline’s bias subtraction step, and additional group-

level destriping steps included as described in Alderson et al. (2023). The ramp-jump detection threshold was set to 10σ , while all other settings were kept at their default values, either as determined by the JWST pipeline (Bushouse et al. 2024) or as specified in Alderson et al. (2023) for the custom steps.

We conducted the stage 2 following Grant et al. (2023). For each integration, the data for each row was divided into segments of 100 pixels. Within each segment, outliers were identified and replaced using the following procedure. A fourth-degree polynomial was fitted to the pixel values, and the residuals and their standard deviation σ were calculated. A pixel was classified as an outlier if the absolute value of its residual exceeded 4σ . This process was iteratively repeated, excluding the identified outliers at each step, until no additional outliers were detected. The identified outliers were then replaced with the values predicted by the fitted polynomial. Following outlier replacement, background subtraction was performed. Each column was fitted with a Gaussian profile, and the centers of the Gaussian fits across all columns were fitted with a second-degree polynomial. Based on this fit, a region centered on the Gaussian peak and extending to 15 times the median of the Gaussian standard deviations was masked. The background value for each column was then estimated as the median of the unmasked region and subtracted. After background subtraction, the outlier cleaning process was repeated. To extract the one-dimensional spectrum, each column was again fitted with a Gaussian profile. The centers of the Gaussian fits across all columns were fitted with a second-degree polynomial. A region extending to six times the median of the Gaussian standard deviations around the Gaussian center was defined, and the pixel values within this region were summed for each column. Finally, the extracted time-series spectra were corrected for wavelength shifts by calculating the median of the spectra over time and using cross-correlation to determine the wavelength shift for each time step. These shifts were then applied to align the spectra in the wavelength direction. Light curves with significant noise were identified by visual inspection and excluded from the set of light curves.

To verify the impact of data reduction on the resulting spectra, an alternative data reduction process was also performed, yielding nearly identical results (Appendix C). Since two independent procedures produced nearly identical spectra, we consider the reduction process to be reliable.

4.2. Light Curve Fitting

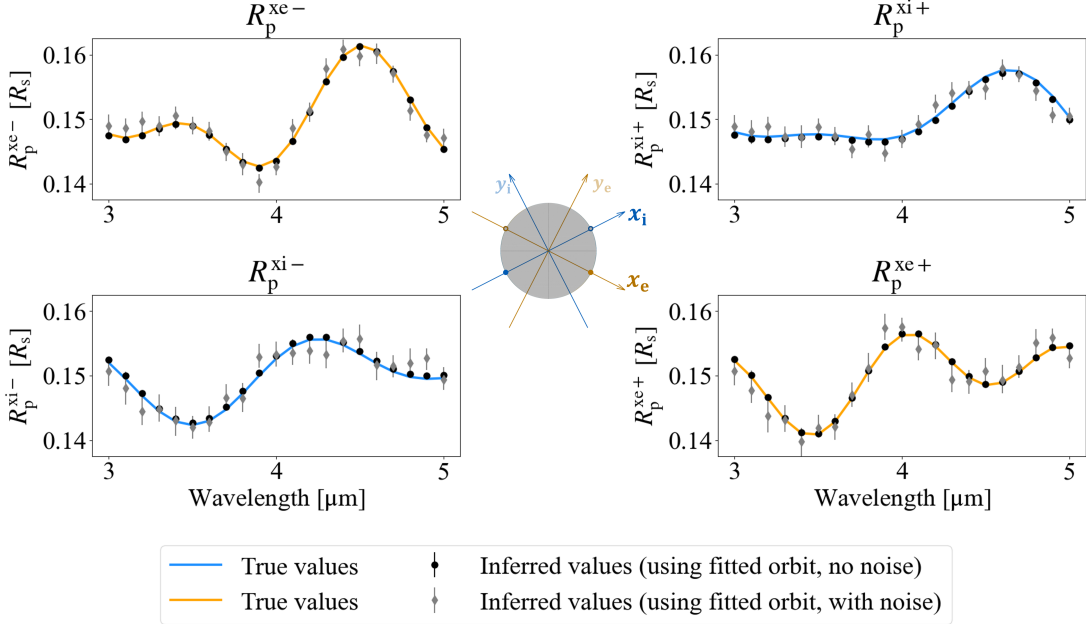


Figure 15. Inferred values of R_p^{xi+} , R_p^{xi-} , R_p^{xe+} , and R_p^{xe-} for an asymmetric planet, based on the MCMC analysis of simulated data. The values were converted using the estimated orbital parameters. The dots represent the median values from the MCMC sampling, while the error bars indicate the 68% credible intervals. Results are shown for both noiseless data and data with added Gaussian noise (mean = 0, standard deviation = 250 ppm), along with the true values. The arrangement of the panels reflects the positional relationship between the regions on the planet contributing to each spectrum, as viewed from the night side. The central panel shows the planet viewed from the night side, along with the x_i -axis, y_i -axis, x_e -axis, and y_e -axis.

We applied binning along the wavelength direction to create light curves with a spectral resolution of $R \sim 100$. This resolution was determined by balancing resolution and precision. Each light curve was normalized by the median value before the transit event, as a mirror-tilt event occurred during the observation (Alderson et al. 2023), altering the baseline before and after the tilt event. The resulting light curves were analyzed by the Hamilton Monte Carlo - No U-Turn Sampler (HMC-NUTS), a specific Markov Chain Monte Carlo (MCMC) algorithm, implemented in NumPyro (Phan et al. 2019). For the transit light curve modeling, a modified version of the `jkepler` code was used, adapted for multi-wavelength analysis. `jkepler` uses `exoplanet_core` library (Foreman-Mackey et al. 2021), which calculates limb darkened transit light curves based on Agol et al. (2020).

This analysis fixed the orbital period at 4.05528 days (Kokori et al. 2023). We assumed the orbital eccentricity of WASP-39 b as zero based on the results by Kammer et al. (2015). Considering the semi-major axis of WASP-39 b, even if the orbital eccentricity is non-zero, the difference between the durations of ingress and egress is less than 1 second. Given the precision of the data, this difference is negligible.

The model parameters are summarized in Table 3. The transit depth k^2 , the central transit time t_0 , the to-

Table 3. Model parameters and their prior distributions in the light curve analysis using MCMC.

Symbol	Description	Prior
k^2	Transit depth \dagger	$\mathcal{U}(0, 0.1)$
t_0	Central transit time [s] $\ast \dagger$	$\mathcal{U}(9000, 10000)$
T_{tot}	Total transit duration [s] \dagger	$\mathcal{U}(9000, 11000)$
T_{full}	Full transit duration [s] \dagger	$\mathcal{U}(1, T_{\text{full}}^{\text{max}})$
c_{base}	Baseline coefficient \dagger	$\mathcal{U}(0.995, 1.005)$
c_{tilt}	Baseline coefficient \dagger	$\mathcal{U}(0.995, 1.0)$
$jitter$	Additional jitter error \dagger	$\mathcal{U}(0, 0.03)$
$q_{1\lambda\text{min}}$	Limb darkening coefficient	$\mathcal{U}(0, 1)$
$q_{2\lambda\text{min}}$	Limb darkening coefficient	$\mathcal{U}(0, 1)$
$q_{1\lambda\text{max}}$	Limb darkening coefficient	$\mathcal{U}(0, 1)$
$q_{2\lambda\text{max}}$	Limb darkening coefficient	$\mathcal{U}(0, 1)$

NOTE— \ast : time from BJD - 59791. \dagger : independently sampled for each wavelength. $\mathcal{U}(a, b)$: the uniform distribution from a to b . $T_{\text{full}}^{\text{max}}$ is defined in equation (33).

tal duration T_{tot} , and the full duration T_{full} were treated as parameters independent of wavelength. To model the transit light curve, we then calculate the semi-major axis a_λ and inclination i_λ at each wavelength using equation (30) and (31). To avoid indeterminate solutions, we impose an upper bound on T_{full} (equation (33)).

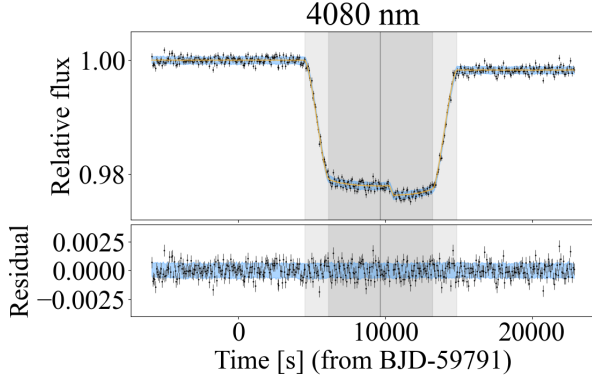


Figure 16. Result of light curve fitting at 4080 nm. The black dots represent the data. The orange line shows the median of the MCMC sampling, and the thin blue region represents the 68% credible interval. The residuals are the differences between the data and the median of the MCMC sampling. The gray vertical line indicates the median of the inferred central transit time, t_0 . The dark gray region represents the median of the inferred total duration, T_{tot} . The light gray region represents the median of the inferred full duration, T_{full} .

We used a quadratic limb darkening model. q_1 and q_2 from Kipping (2013) were sampled and then converted to u_1 and u_2 . Since q_1 and q_2 are expected to exhibit similar values for nearby wavelengths, we incorporated this by assuming a simple linear wavelength dependence for q_1 and q_2 . To implement this, q_1 and q_2 at minimum wavelength, $q_{1\lambda_{\text{min}}}$ and $q_{2\lambda_{\text{min}}}$, and q_1 and q_2 at maximum wavelength, $q_{1\lambda_{\text{max}}}$ and $q_{2\lambda_{\text{max}}}$, were sampled using uniform distributions between 0 and 1.

Regarding the parameterization of limb darkening coefficients, Coulombe et al. (2024) demonstrated that using q_1 and q_2 could introduce wavelength-dependent biases in the inferred transit depths. We address this issue in Appendix D by comparing the results with those obtained from additional light curve fits, where u_1 and u_2 were treated as free parameters for each wavelength. We did not detect the wavelength-dependent biases in the inferred transit depths. In addition, while the uncertainty in the resulting spectra was larger when no wavelength dependence was assumed for u_1 and u_2 , the overall shape of the spectra remained consistent with the results obtained using the linear wavelength dependence for q_1 and q_2 .

The baseline of light curves was assumed to be constant. However, the mirror-tilt event during the observation (Alderson et al. 2023) changed the baseline before and after the tilt event. We set the baseline before the tilt event as c_{base} , and after the tilt event as $c_{\text{base}} \times c_{\text{tilt}}$.

These baseline constants were also treated as parameters independent of wavelength.

The likelihood of the light-curve data was modeled as a product of normal distributions for each wavelength. The means of these distributions were given by (transit light curve model) \times (baseline) and the variances are given by $(\text{data error})^2 + (\text{jitter})^2$. The *jitter* was treated as an independent parameter for each wavelength.

An example of the fitted light curve and its residuals obtained by the above procedure is shown in Figure 16. The variance of the residuals remains nearly constant before and after the transit, as well as before and after the tilt event, indicating that the light curve is well-fitted.

Figure 17 shows the inferred values of all the parameters in the light curve model obtained from the MCMC sampling. The dots represent the median values of the MCMC sampling, and the error bars indicate the 68% credible intervals. For parameters independently sampled for each wavelength, the values for all wavelength bins are shown, allowing us to observe the chromatic variation of k^2 , t_0 , T_{tot} , and T_{full} . For the limb darkening coefficients, the inferred values at the minimum and maximum wavelengths, along with the wavelength dependence for each sampling, are shown. Additionally, u_1 and u_2 , converted from q_1 and q_2 , are also displayed.

4.3. Planetary Radius Spectra in Four Directions

By assuming the orbit of the planet’s center of mass and the wavelength dependence of the host star’s radius, we can obtain the spectra of R_{p}^{xi+} , R_{p}^{xi-} , R_{p}^{xe+} , and R_{p}^{xe-} from the results of the light curve fitting.

The orbit of the planet’s center of mass cannot be determined solely by transit light curves because they are affected by atmospheric asymmetries. However, as discussed in Dobbs-Dixon et al. (2012), the orbital parameters determined from the data at wavelengths that exhibit small radii are considered to be close to the orbital parameters of the center of mass. Here, we use wavelengths that exhibit radii smaller than the 10th percentile to determine the orbit of the planet’s center of mass. For each of those wavelength bins, we calculated the median of the orbital parameters obtained from the MCMC sampling and then used the average of these values as the orbital parameters of the center of mass. As a result, we determined the mean wavelength of these bins as $\lambda_0 = 3821.5$ nm, the semi-major axis as $11.367 R_{\text{s}}(\lambda_0)$, the impact parameter as 0.45284, and the central transit time as 9681.4 s from BJD - 59791 as the orbital parameters of the planet’s center of mass.

Although the wavelength-dependent stellar radius, $R_{\text{s}}(\lambda)$, is challenging to estimate with the precision re-

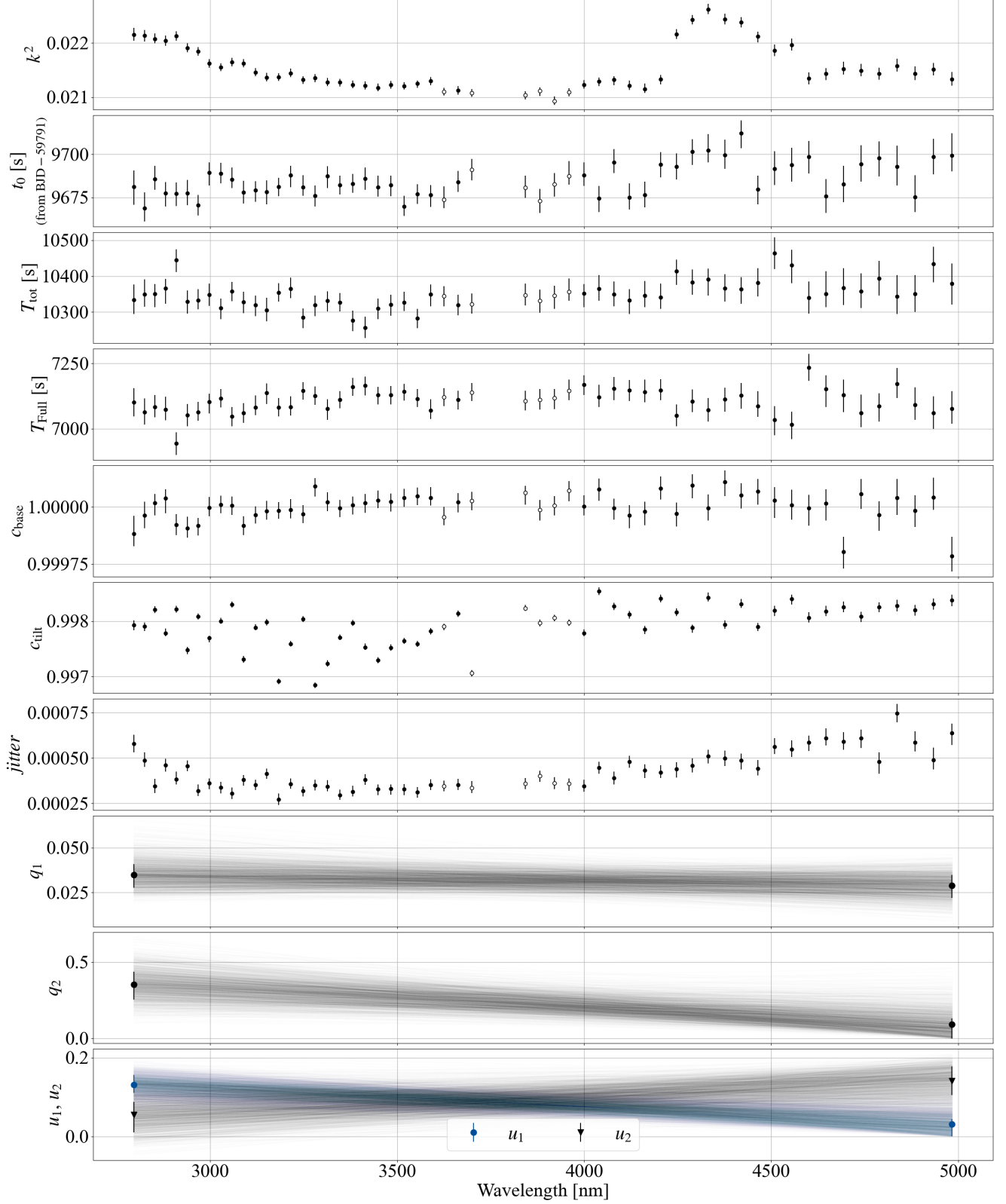


Figure 17. Inferred values of all the parameters in the light curve model obtained from the MCMC sampling. For the limb darkening coefficients, the inferred values at the minimum and maximum wavelengths, along with the wavelength dependence for each sampling, are shown. u_1 and u_2 , converted from q_1 and q_2 , are also displayed. The dots represent the median values of the MCMC sampling, and the error bars indicate the 68% credible intervals. The white-filled dots indicate the wavelengths that exhibit radii smaller than the 10th percentile and are used to determine the orbit of the planet's center of mass.

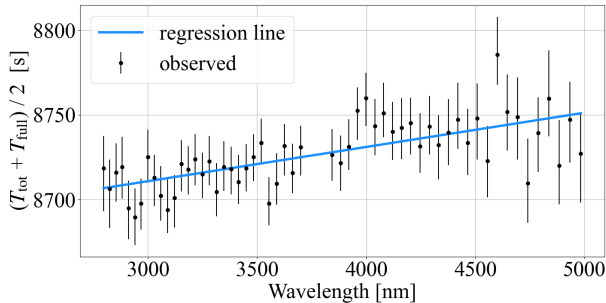


Figure 18. Inferred value of $(T_{\text{tot}} + T_{\text{full}})/2$ and its linear regression line (blue solid line). The dots with error bars represent the median values of the MCMC sampling and the 68% credible intervals.

quired for this method, the transit duration provides important information about it (§2.6). We observed that the transit duration gradually increases with wavelength, as shown in Figure 18.

The natural logarithms of the Bayesian evidences for the constant model (M1) and the linear model (M2: constant + slope \times wavelength) were -246.2 and -234.0 , respectively, indicating that M2 is preferred over M1 (Gregory 2005). The prior distributions used in this analysis were as follows. For the constant term, which represents the value at λ_0 , a uniform prior was set as $\mathcal{U}(\min(\mathbf{y}), \max(\mathbf{y})) = \mathcal{U}(8690.1 \text{ s}, 8786.2 \text{ s})$. For the slope, the prior distribution was set as

$$\mathcal{U}\left(-2 \cdot \frac{\max(\mathbf{y}) - \min(\mathbf{y})}{\max(\mathbf{x}) - \min(\mathbf{x})}, 2 \cdot \frac{\max(\mathbf{y}) - \min(\mathbf{y})}{\max(\mathbf{x}) - \min(\mathbf{x})}\right) \\ = \mathcal{U}(-87.86 \text{ s}/\mu\text{m}, 87.86 \text{ s}/\mu\text{m}),$$

where \mathbf{y} is the mean of the samples of $(T_{\text{tot}} + T_{\text{full}})/2$ for each wavelength, and \mathbf{x} is the wavelength. This linear trend can be attributed to both the wavelength dependence of the planet’s atmospheric asymmetries and the host star’s radius. Here, we attribute the trend to the wavelength dependence of the host star’s radius and estimate $\alpha(\lambda)$ based on this trend.

We can use equation (29) to derive $\alpha(\lambda)$. For $T_{\text{bc}}(\lambda)$, we used the linear regression of $(T_{\text{tot}} + T_{\text{full}})/2$ (see Appendix A). To perform a linear regression robust to outliers, we used the Student’s t-distribution as the likelihood function for the MCMC sampling. The free parameters in this regression were the slope of the line, the value at $\lambda = \lambda_0$, and the scale and degrees of freedom of the Student’s t-distribution. We then obtained $\alpha(\lambda) = R_s(\lambda)/R_s(\lambda_0) \sim 1 + 1.83 \times 10^{-6}(\lambda - \lambda_0)$, where the wavelengths λ and λ_0 are in units of nanometers. This means the host star’s radius increases at a rate of $0.183\% \mu\text{m}^{-1}$ in the wavelength range of approximately 3 to 5 μm . As discussed in Appendix B, simula-

tions using the PHOENIX model (Husser et al. 2013) suggest that a star with an effective temperature of 5500 K, surface gravity $\log g [\text{cgs}] = 4.5$, and metallicity $[\text{Fe}/\text{H}] = 0.0$ can exhibit a stellar radius change rate of approximately $0.12\% \mu\text{m}^{-1}$ within this wavelength range. WASP-39, a G8-type star, has an effective temperature of $5485 \pm 50 \text{ K}$, surface gravity $\log g [\text{cgs}] = 4.41 \pm 0.15$, and metallicity $[\text{Fe}/\text{H}] = 0.01 \pm 0.09$ (Mancini et al. 2018). These properties are similar to the star discussed in Appendix B, making the derived rate of $0.183\% \mu\text{m}^{-1}$ for WASP-39 possible. In the following discussion, we will base our analysis on the value of $\alpha(\lambda)$ estimated here. However, since the linear trend of $(T_{\text{tot}}(\lambda) + T_{\text{full}}(\lambda))/2$ could also be attributed to atmospheric asymmetries, we will also display the case where $\alpha(\lambda) = 1$ in the figures.

Figure 19 shows the time-related parameters of the conventional transit model, the timings of ingress (t_i), the timing of egress (t_e), and the duration of ingress or egress ($\tau_i = \tau_e$). We plot the predicted values for the case of no asymmetries (a completely symmetrical atmosphere), which were calculated using eqs. (14) and (15) in Winn (2010) with the median values of k^2 from MCMC sampling, along with the semi-major axis, impact parameter, and central transit time of the planet’s center of mass. As shown in this figure, the deviations from the symmetrical atmosphere are observed to be larger in the timings of ingress and egress than in the duration.

Figure 20 shows the center displacements of the planet’s shadow disk, $\Delta c_{i,xi}$, $\Delta c_{i,yi}$, $\Delta c_{e,xe}$ and $\Delta c_{e,ye}$. The colored dots indicate the case using $\alpha(\lambda)$ estimated from $(T_{\text{tot}} + T_{\text{full}})/2$, while the small gray dots indicate the case using $\alpha(\lambda) = 1$. The precision of $\Delta c_{i,xi}$ and $\Delta c_{e,xe}$ is much higher than that of $\Delta c_{i,yi}$ and $\Delta c_{e,ye}$. By comparing the wavelength dependence of the plots in Figures 19 and 20, it becomes clear that the shapes of t_i and $\Delta c_{i,xi}$, as well as t_e and $\Delta c_{e,xe}$, are almost identical, although their signs are reversed. The bottom panels of Figure 20 show the distribution of displacement values converted from MCMC sampling at selected wavelengths. The clear distribution along the host star’s edge indicates that $\Delta c_{i,xi}$ and $\Delta c_{e,xe}$ are well determined by the data.

Finally, we convert $\Delta c_{i,xi}$ to the spectra of R_p^{xi+} and R_p^{xi-} , and $\Delta c_{e,xe}$ to the spectra of R_p^{xe+} and R_p^{xe-} , as shown in Figure 21. The central panel of Figure 21 illustrates the corresponding positions on the planet for these spectra. Since these values represent projected lengths of the planet’s shadow disk onto the x_i -axis or x_e -axis, measured from the planet’s center of mass, rather than exact radii (Figure 4), the uncertainties in

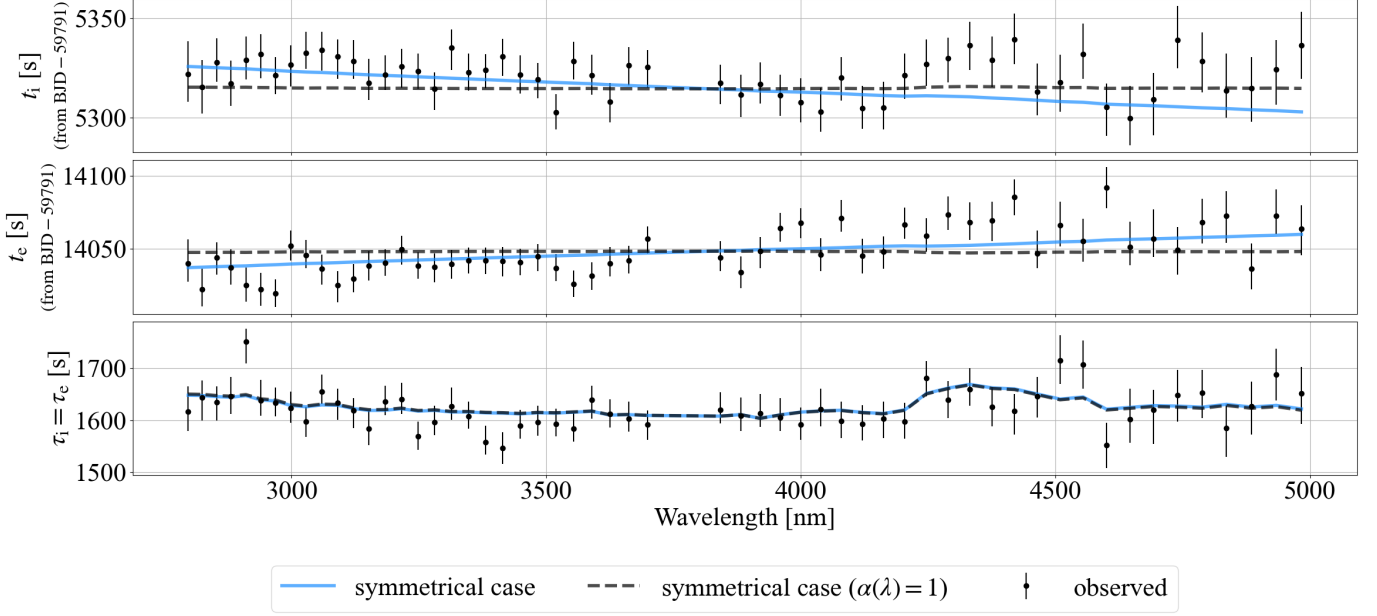


Figure 19. Inferred values of the timing of ingress t_i , the timing of egress t_e , and the duration of ingress and egress τ . The dots with error bars represent the median values from the MCMC sampling with 68% credible intervals. The solid blue lines (using $\alpha(\lambda)$ estimated from $(T_{\text{tot}} + T_{\text{full}})/2$) and the dashed gray lines (using $\alpha(\lambda) = 1$) represent these values in the case of a completely symmetrical atmosphere, derived from the orbital parameters of the planet’s center of mass and the inferred planetary radii.

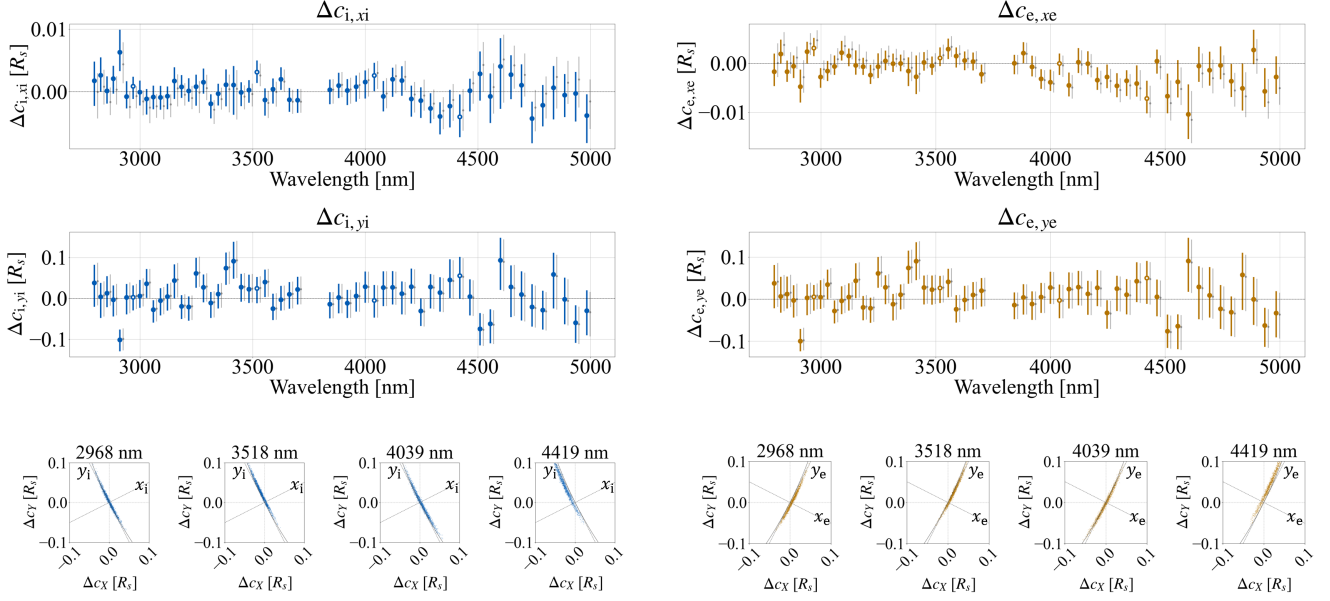


Figure 20. Inferred center displacements of the planet’s shadow disk: $\Delta c_{i,x_i}$, $\Delta c_{i,y_i}$, $\Delta c_{e,x_e}$ and $\Delta c_{e,y_e}$. The dots represent the median values from MCMC sampling, and the error bars represent the 68% credible intervals. The colored dots indicate the case using $\alpha(\lambda)$ estimated from $(T_{\text{tot}} + T_{\text{full}})/2$, while the small gray dots indicate the case using $\alpha(\lambda) = 1$. The bottom panels show the distribution of displacement values converted from MCMC sampling at selected wavelengths, which are indicated by white-filled dots in the top and second panels. The dotted lines represent the X -axis and Y -axis, and the dashed lines represent the x_i -axis and y_i -axis for the left-side four panels, and the x_e -axis and y_e -axis for the right-side four panels. The edge of the host star is plotted as black solid lines, which are nearly aligned with the y_i -axis or y_e -axis. The distribution along the host star’s edge is clearly visible.

Δc shown in Figure 20 are also illustrated to indicate

the uncertainties in the positions from which these values are projected.

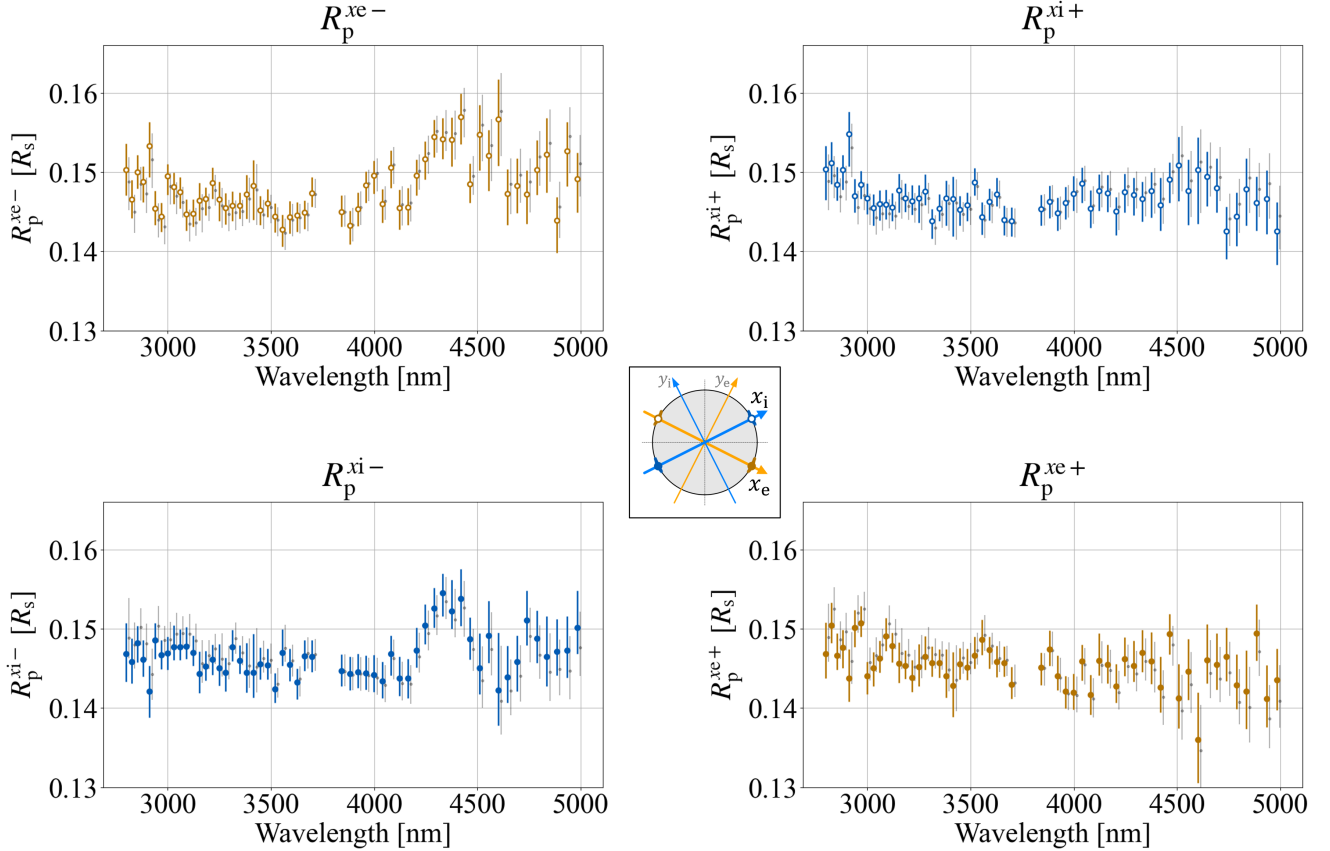


Figure 21. Spectra of R_p^{xe-} (top left), R_p^{xi+} (top right), R_p^{xi-} (bottom left), and R_p^{xe+} (bottom right). The dots with error bars represent the median values from the MCMC sampling with 68% credible intervals. The colored dots indicate the case using $\alpha(\lambda)$ estimated from $(T_{\text{tot}} + T_{\text{full}})/2$, while the small gray dots indicate the case using $\alpha(\lambda) = 1$. The central panel shows the positions on the planet that correspond to these spectra, along with the x_i -axis, y_i -axis, x_e -axis, and y_e -axis. The color of points indicating those positions corresponds to the color of dots in each spectrum. Since these spectra are not exact radii but rather projected lengths of the planet’s shadow disk onto the x_i -axis or x_e -axis, measured from the planet’s center of mass (Figure 4), the uncertainties of Δc shown in Figure 20 are also illustrated to indicate the uncertainties of positions from which these values are projected.

Clear differences in the shape of these spectra are observed. In particular, R_p^{xi+} and R_p^{xe+} (the morning side) have flatter spectra than R_p^{xe-} and R_p^{xi-} (the evening side). We can also see differences between the spectra of R_p^{xe-} and R_p^{xi+} (the north side) and those of R_p^{xi-} and R_p^{xe+} (the south side). We will discuss these differences using atmospheric models in the next section.

5. IMPLICATION TO THE PLANETARY ATMOSPHERE

In the previous section, we decomposed the light curve of WASP-39 b into spectra in four directions (Figure 21). In this section, we will analyze each spectrum using atmospheric retrieval and interpret the results. We will focus on the spectra calculated using the wavelength dependence of the stellar radius, $\alpha(\lambda)$, estimated from the linear trend of $(T_{\text{tot}} + T_{\text{full}})/2$.

5.1. Atmospheric Retrieval

The spectra in four directions were analyzed by HMC-NUTS, implemented in NumPyro (Phan et al. 2019). For the transmission spectrum modeling, we used ExoJAX, a differentiable planet spectral model (Kawahara et al. 2022, Kawahara et al. submitted).

We assumed a constant temperature profile characterized by T and a gray cloud that is opaque below a certain pressure, independent of wavelength. The collision-induced absorption (CIA) of the hydrogen and helium atmosphere was also incorporated (H_2 - H_2 and H_2 -He, Richard et al. 2012; Karman et al. 2019). Molecular species included were CO, CO_2 , H_2O , and CH_4 (HITEMP, Rothman et al. 2010; Hargreaves et al. 2020), H_2S (ExoMol/AYT2, Azzam et al. 2016; Chubb et al. 2018), SO_2 (ExoMol/ExoAmes, Underwood et al.

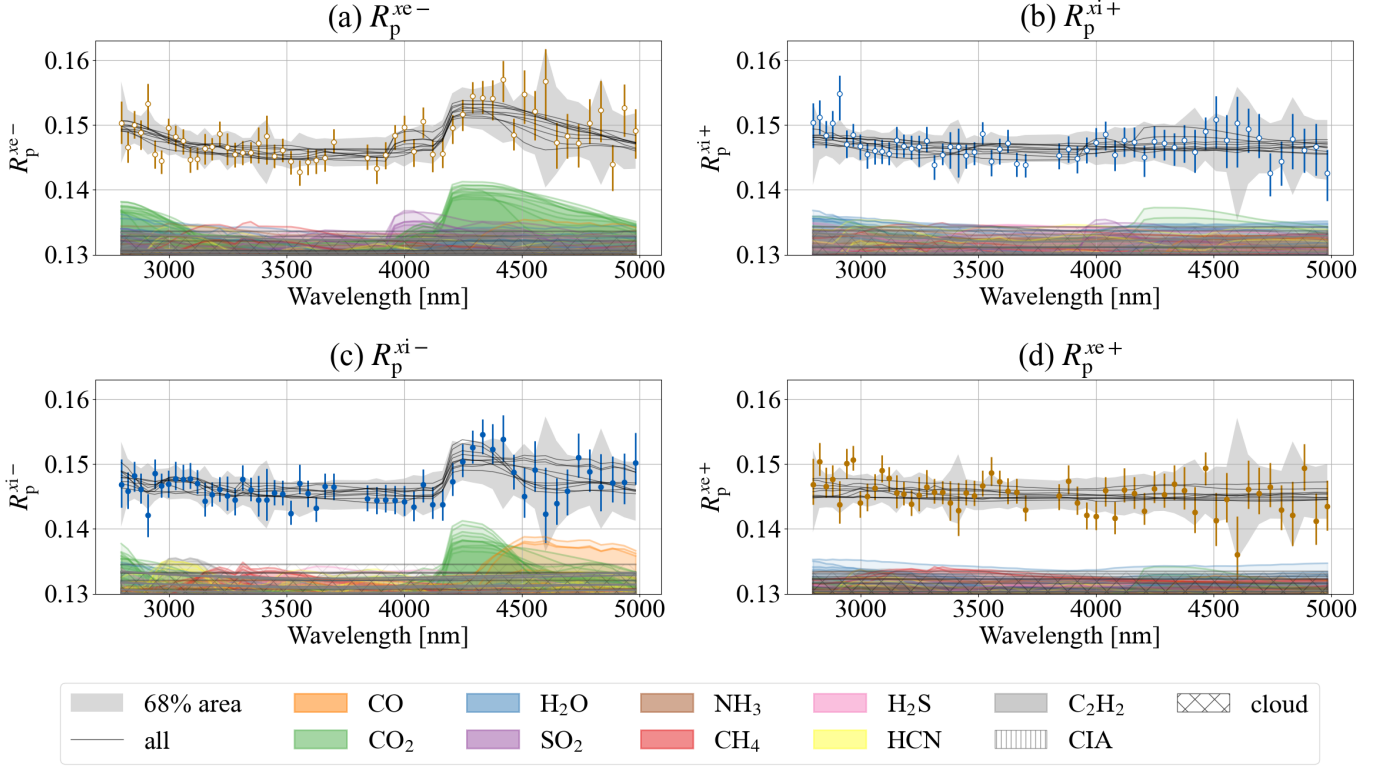


Figure 22. Results of MCMC sampling for the spectra: (a) R_p^{xe-} , (b) R_p^{xi+} , (c) R_p^{xi-} , and (d) R_p^{xe+} . The dots with error bars represent the spectra shown in Figure 21, calculated using $\alpha(\lambda)$ estimated from $(T_{\text{tot}} + T_{\text{full}})/2$. The grey regions in each panel indicate the 68% credible intervals for each spectrum from the MCMC sampling. The black lines in each panel represent ten randomly selected sampled models. The contributions of each molecule, grey clouds, and CIA to these models are also shown as colored or hatched shading, with an offset of $-0.01 R_s$.

2016; Tóbiás et al. 2018; Rothman et al. 2013), NH_3 (ExoMol/CoYuTe, Al Derzi et al. 2015; Coles et al. 2019), HCN (ExoMol/Harris, Harris et al. 2006; Barber et al. 2014; Mehrotra et al. 1985; Cohen & Wilson 1973; Charrón et al. 1980), and C_2H_2 (ExoMol/aCeTY, Chubb et al. 2020; Wilzewski et al. 2016; Gordon et al. 2017).

The free parameters in the MCMC sampling were the temperature T , the logarithm of the pressure at the cloud top $\log P_{\text{cloud}}$, the logarithm of the volume mixing ratio (VMR) of nine molecular species, the radius of the host star R_s , the planetary mass M_p , and the planetary radius R_p at an altitude of 10 bar. R_s , M_p , and R_p at 10 bar were assumed to be common across all four limbs, while the other parameters were treated independently for each limb. The VMRs of H_2 and He were assumed to be the remaining 6/7 and 1/7, respectively, after subtracting the VMRs of the nine aforementioned molecules.

The prior distributions of each parameter are summarized in Table 4. The prior distributions for R_s and M_p were based on Mancini et al. (2018). We fixed the radial

velocity of the system at -87.3 km/s (Esparza-Borges et al. 2023).

The model spectra were derived from the opacity of the atmosphere, which ranged from 10 bar to 10^{-11} bar and was divided logarithmically into 120 layers. The spectra were initially calculated at a spectral resolution of 6000 and then broadened to a resolution of 2700, approximately matching the instrumental spectral resolution, using Gaussian functions. Finally, by applying binning, we reduced the model spectra to a spectral resolution of approximately 100.

The likelihood function for this MCMC sampling was modeled as the product of multivariate normal distributions for each spectrum. The means of these distributions were the model spectra for each direction. The covariance matrices of these distributions represent the variances of the values in each wavelength bin along the diagonal and the covariances between pairs of wavelength bins in the off-diagonal elements. These covariance matrices for each spectrum were obtained from the MCMC sampling in the previous section.

Figure 22 shows the 68% credible intervals of each spectrum from the MCMC sampling. The arrangement

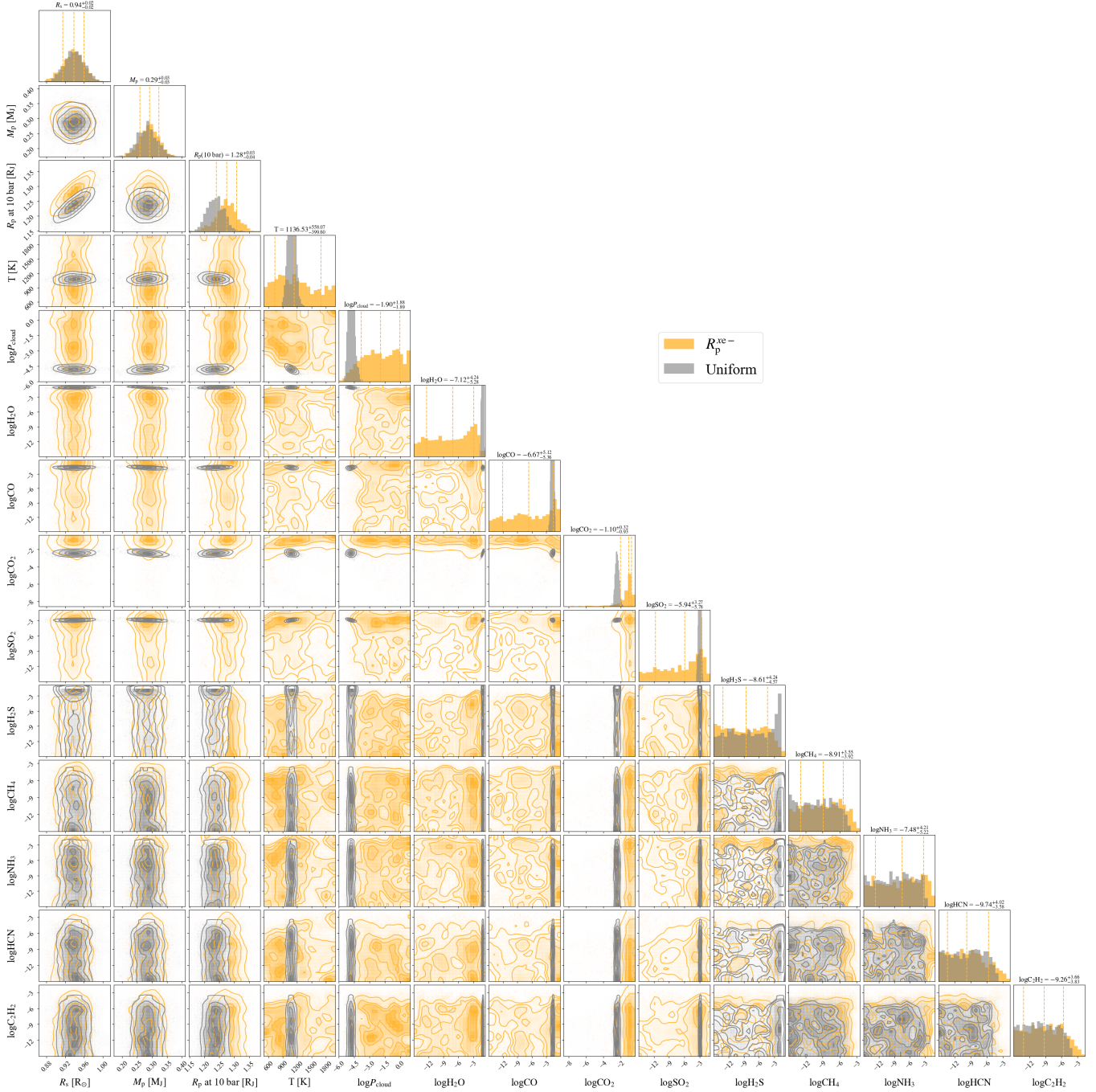


Figure 23. Posterior distributions of each parameter for the R_p^{xe-} spectrum (orange). The R_p at 10 bar is common for all four limbs (Figure 23 – 26). The posterior distributions from the analysis with the intrinsic spectral resolution (~ 2700), assuming a uniform atmosphere (Kawahara et al. submitted), are overlaid for reference (gray).

of R_p^{xe-} (Panel (a)), R_p^{xi+} (Panel (b)), R_p^{xi-} (Panel (c)), and R_p^{xe+} (Panel (d)) is the same as in Figure 21. The black lines in each panel represent ten randomly selected sampled models. The contributions of each molecule, gray clouds, and CIA to these models are also shown as colored or hatched shading, with an offset of $-0.01 R_s$.

Figure 23 (R_p^{xe-}), 24 (R_p^{xi+}), 25 (R_p^{xi-}), and 26 (R_p^{xe+}) show the posterior distributions of each parameter for each spectrum. In these figures, the posterior distributions from the analysis with the intrinsic spectral resolution (~ 2700), assuming a uniform atmosphere (Kawahara et al. submitted), are overlaid for reference.

5.2. Insights from the Atmospheric Retrieval

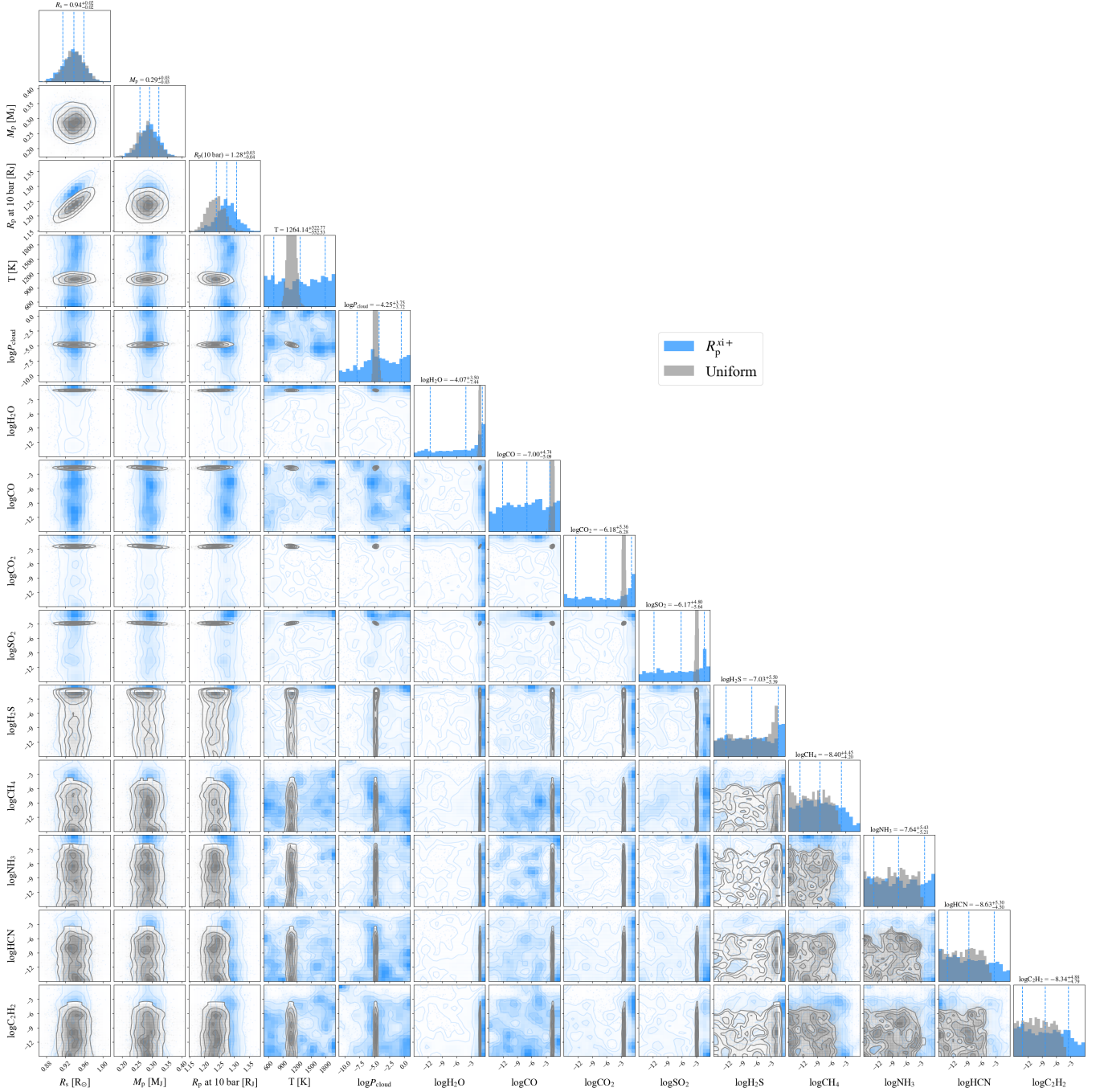


Figure 24. Posterior distributions of each parameter for the R_p^{xi+} spectrum (blue). The R_p at 10 bar is common for all four limbs (Figure 23–26). The posterior distributions from the analysis with the intrinsic spectral resolution (~ 2700), assuming a uniform atmosphere (Kawahara et al. submitted), are overlaid for reference (gray).

We observe that the spectra on the morning side (Panel (b) R_p^{xi+} and (d) R_p^{xe+} of Figure 22) are flatter than those on the evening side (Panel (a) R_p^{xe-} and (c) R_p^{xi-} of Figure 22). In both evening-side spectra, absorption features from CO_2 are evident.

Recently, Espinoza et al. (2024) constrained the temperature of the morning limb to 889^{+54}_{-65} and that of the

evening limb to 1068^{+43}_{-55} . In contrast, our analysis did not yield constraints on the limb temperatures in any direction. This discrepancy may arise from differences in the model used for retrieval; for instance, we employed a free chemistry model, whereas Espinoza et al. (2024) assumed chemical equilibrium.

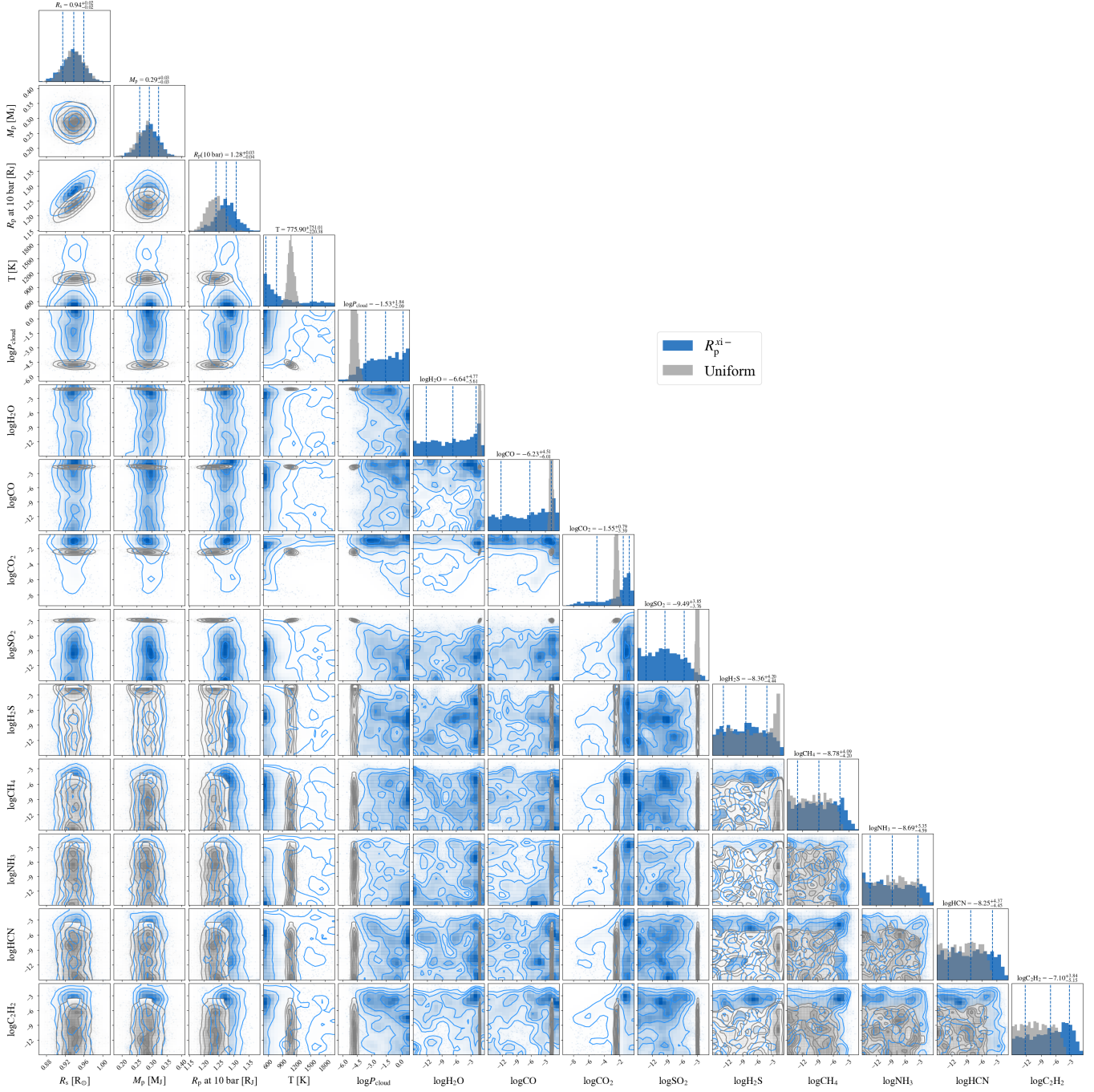


Figure 25. Posterior distributions of each parameter for the R_p^{xi-} spectrum (dark blue). The R_p at 10 bar is common for all four limbs (Figure 23–26). The posterior distributions from the analysis with the intrinsic spectral resolution (~ 2700), assuming a uniform atmosphere (Kawahara et al. submitted), are overlaid for reference (gray).

The atmospheric retrieval constrained the $\log(\text{CO}_2)$ in the negative x_e direction to $-1.1^{+0.3}_{-0.9}$ (Figure 23) and in the negative x_i direction to $-1.55^{+0.8}_{-3.4}$ (Figure 25). Although some models in Figure 22 suggest the presence of other molecules, such as SO_2 (around 4000 nm in Panel (a) R_p^{xe-}) and CO (around 4500 ~ 5000 nm in Panel (c) R_p^{xi-}), the VMRs of these molecules were not

constrained. These VMRs might be constrained with increased data precision or by using spectra from other wavelength ranges.

Although the inferred VMRs of CO_2 are relatively high, they are consistent with the high metallicity reported in previous studies. For instance, Alderson et al. (2023) suggests 3 to 10 times solar metallicity, and Con-

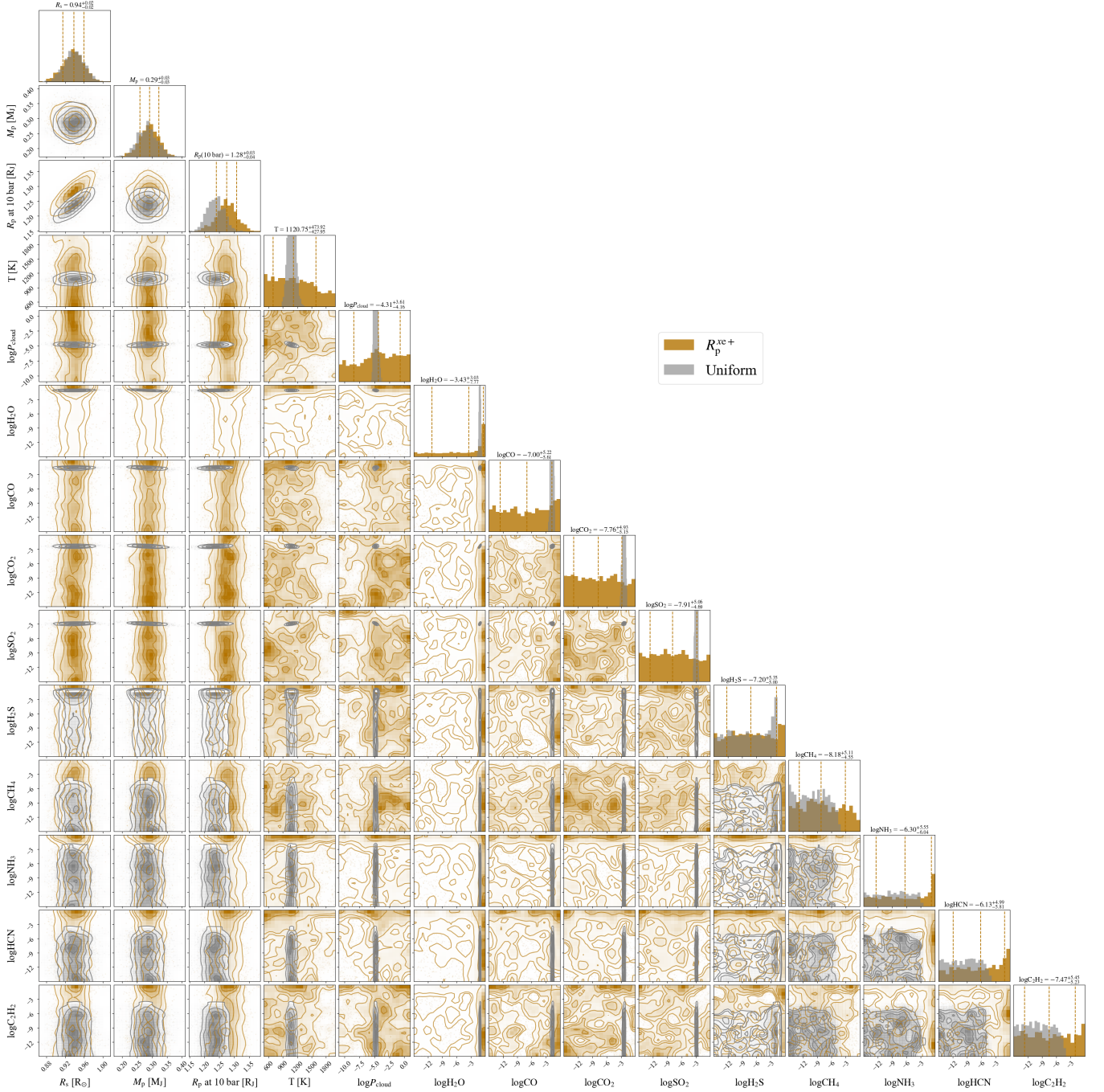


Figure 26. Posterior distributions of each parameter for the $R_p^{\text{sc}+}$ spectrum (dark orange). The R_p at 10 bar is common for all four limbs (Figure 23–26). The posterior distributions from the analysis with the intrinsic spectral resolution (~ 2700), assuming a uniform atmosphere (Kawahara et al. submitted), are overlaid for reference (gray).

stantinou & Madhusudhan (2024) reports $20.1^{+10.5}_{-8.1} \times$ and $28.2^{+16.3}_{-12.1} \times$ solar abundances for O/H and C/H, respectively. In our other analysis of these data, using the native spectral resolution of NIRSpect/G395H (~ 2700) and assuming a uniform atmosphere (Kawahara et al. submitted), we also found a relatively high VMR of $\log(\text{CO}_2) = -2.4 \pm 0.2$.

The VMR of CO_2 was not well constrained in the positive x_i and x_e directions, which correspond to the morning side. This suggests that CO_2 is more abundant on the evening limb than on the morning limb. In this context, the higher VMRs of CO_2 observed on the evening limb, compared to those expected under the assumption of a uniform atmosphere, can be naturally understood as

Table 4. Model parameters and their prior distributions in the atmospheric retrieval analysis using MCMC.

Symbol	Description	Prior
R_s *	Host star’s radius (R_\odot)	$\mathcal{N}(0.939, 0.022)$
M_p *	Planetary mass (M_J)	$\mathcal{N}(0.281, 0.032)$
R_p at 10 bar *	height at 10 bar (R_J)	$\mathcal{U}(1.0, 1.5)$
T	temperature (K)	$\mathcal{U}(500, 2000)$
$\log P_{\text{cloud}}$	cloud top pressure (bar)	$\mathcal{U}(-11.0, 1.0)$
$\log \text{H}_2\text{O}$	VMR of H_2O	$\mathcal{U}(-15.0, 0.0)$
$\log \text{CO}$	VMR of CO	$\mathcal{U}(-15.0, 0.0)$
$\log \text{CO}_2$	VMR of CO_2	$\mathcal{U}(-15.0, 0.0)$
$\log \text{SO}_2$	VMR of SO_2	$\mathcal{U}(-15.0, 0.0)$
$\log \text{H}_2\text{S}$	VMR of H_2S	$\mathcal{U}(-15.0, 0.0)$
$\log \text{CH}_4$	VMR of CH_4	$\mathcal{U}(-15.0, 0.0)$
$\log \text{NH}_3$	VMR of NH_3	$\mathcal{U}(-15.0, 0.0)$
$\log \text{HCN}$	VMR of HCN	$\mathcal{U}(-15.0, 0.0)$
$\log \text{C}_2\text{H}_2$	VMR of C_2H_2	$\mathcal{U}(-15.0, 0.0)$

NOTE—*: common for all the four limbs. $\mathcal{N}(a, b)$: the normal distribution with a mean of a and a standard deviation of b , truncated to ensure that the values are non-negative. $\mathcal{U}(a, b)$: the uniform distribution from a to b . $\log X$: $\log_{10} X$

a result of CO_2 being more concentrated on the evening side. Since CO_2 is thought to be produced both thermochemically and photochemically (Fleury et al. 2020), the higher abundance of CO_2 on the evening limb could be attributed to photochemical production on the dayside, followed by transport via eastward zonal wind.

However, the posterior distribution of the VMR of CO_2 in the positive x_1 direction (Figure 24) indicates a higher probability of elevated VMRs. Given that differences in temperature can affect the strength of absorption features in the transmission spectrum (Agúndez et al. 2014), the observed differences in the CO_2 absorption features might be attributed to temperature differences between the morning and evening limbs.

Next, we consider SO_2 , which has been detected in analyses assuming a uniform atmosphere (e.g. Alderson et al. 2023; Powell et al. 2024, Kawahara et al. submitted). Simulations have shown that the formation of SO_2 can be explained by photochemistry (Tsai et al. 2023b).

The posterior distributions suggest that SO_2 is more likely to be present on the north limb (Figure 23 R_p^{xe-} and 24 R_p^{xi+}) than on the south limb (Figure 25 R_p^{xi-} and 26 R_p^{xe+}), although the difference is slight. As discussed in §2.2, the north limb receives more intense illumination from the host star than the south limb, which could result in a higher abundance of SO_2 on the brighter north limb due to enhanced photochemi-

cal production. However, this hypothesis contrasts with the prediction by Tsai et al. (2023a), who suggested that SO_2 would accumulate on the nightside due to the effects of horizontal transport by zonal wind.

If CO_2 and SO_2 are both abundant on the evening limb slightly offset from the terminator on the dayside (negative x_e direction), while CO_2 remains abundant but SO_2 is depleted on the evening limb slightly offset from the terminator on the nightside (negative x_1 direction), one possible explanation, though speculative, is a difference in the dissociation timescales of these molecules. In this scenario, the dissociation timescale of CO_2 would be longer than that of SO_2 , allowing CO_2 to be transported from the dayside to the nightside, while SO_2 would dissociate before reaching the nightside. Further investigation will be required to explore this possibility and gain a deeper understanding of the atmospheric dynamics.

6. DISCUSSION

We explored the connection between chromatic transit variation (CTV) and atmospheric asymmetries on planetary limbs. Understanding this connection helps leverage high-precision transmission spectroscopic data, such as those obtained with JWST. While more flexible models may become necessary as data quality improves, this understanding provides a valuable foundation for developing optimized models to analyze atmospheric inhomogeneities using transmission spectroscopy.

In §2, we discussed two potential sources of uncertainty in this method: the orbit of the planet’s center of mass and the wavelength dependence of the host star’s radius. The analysis in §4 did not account for errors in these values. As noted in §2, estimating these uncertainties is currently nearly impossible. However, incorporating these uncertainties into inferred quantities, such as temperatures and volume mixing ratios (VMRs), is essential for making the results more robust. Addressing this challenge is an important task for future work.

The method introduced in this paper enables the investigation of atmospheric properties, particularly the distribution of molecules, around the terminator of close-in exoplanets. Thanks to the wide wavelength coverage and exceptional precision of JWST’s transmission spectra, we can explore the distribution of key molecules, such as SO_2 , across the planet’s atmosphere. By combining this method with complementary observational techniques, such as phase curves and secondary eclipse observations, we can significantly enhance our understanding of exoplanetary atmospheres.

7. SUMMARY

This paper presented a new method for exploring atmospheric inhomogeneity in exoplanets by analyzing chromatic transit variation (CTV). We found that the timings of ingress and egress reflect asymmetries perpendicular to the host star’s edge, while the durations of ingress and egress reflect asymmetries perpendicular to the planet’s orbital motion. Based on these insights, we derived formulations that convert the transit depth k^2 and contact times t_{I} , t_{II} , t_{III} , and t_{IV} into the spectra of projected lengths of the planet’s shadow disk, measured from the planet’s center of mass in four different directions. This approach enables us to divide both the morning and evening limbs into two regions each: one slightly offset from the day-night terminator on the day-side, and one on the nightside.

We applied the method to JWST’s NIRSpec/G395H observation of WASP-39b and found a higher abundance of CO_2 on the evening limb compared to the morning limb. Our results also indicate a greater probability of SO_2 on the limb slightly offset from the terminator on the dayside relative to the nightside. These results should be interpreted in the context of the photochemical processes and atmospheric circulation.

This work is based on observations made with the NASA/ESA/CSA James Webb Space Telescope. The data were obtained from the Mikulski Archive for Space Telescopes at the Space Telescope Science Institute, which is operated by the Association of Universities for Research in Astronomy, Inc., under NASA contract NAS 5-03127 for JWST. The specific observations analyzed can be accessed via [10.17909/7559-ne05](https://doi.org/10.17909/7559-ne05). These observations are associated with program ERS-1366. The authors acknowledge the Transiting Exoplanet Community Early Release Science Program team for developing their observing program with a zero-exclusive-access period. We thank Yui Kasagi, Shota Miyazaki, and Hibiki Yama for the fruitful discussions. This study was supported by JSPS KAKENHI grant nos. 21H04998, 23H00133, 23H01224 (H.K.), 21K13984, 22H05150, 23H01224 (Y.K.), 21H04998 (K.M.)

Facility: JWST

Software: ExoTIC-JEDI (Alderson et al. 2022), jwst (Bushouse et al. 2024), jkepler, ExoJAX (Kawahara et al. 2022), jaxoplanet (Hattori et al. 2024), JAX (Bradbury et al. 2018), Numpyro (Bingham et al. 2019; Phan et al. 2019), Numpy (Harris et al. 2020), xarray (Hoyer et al. 2024), matplotlib (Hunter 2007), catwoman (Jones & Espinoza 2020; Espinoza & Jones 2021)

APPENDIX

A. TIMING OF INGRESS AND EGRESS

We defined the timing of ingress as

$$\begin{aligned} t_{\text{i}} &= (t_{\text{I}} + t_{\text{II}})/2 \\ &= t_0 - \frac{T_{\text{tot}} + T_{\text{full}}}{4}, \end{aligned} \tag{A1}$$

and the timing of egress as

$$\begin{aligned} t_{\text{e}} &= (t_{\text{III}} + t_{\text{IV}})/2 \\ &= t_0 + \frac{T_{\text{tot}} + T_{\text{full}}}{4}. \end{aligned} \tag{A2}$$

These values differ slightly from t'_{i} and t'_{e} , which are the times when the center of the planet’s shadow disk intersects the host star’s edge. While this difference does not affect the formulation in §2, we discuss it here for a better understanding of the method.

For simplicity, we assume the planet’s shadow at wavelength λ has a transit depth of $k(\lambda)^2$ and follows a circular orbit with a semi-major axis a_λ , impact parameter b_λ , and central transit time $t_0(\lambda)$. The values of a_λ and b_λ can be

estimated from $T_{\text{tot}}(\lambda)$, $T_{\text{full}}(\lambda)$, and $k(\lambda)^2$. From eqs. (14) and (15) in Winn (2010), $T_{\text{tot}}(\lambda)$, $T_{\text{full}}(\lambda)$ are given by

$$T_{\text{tot}} = \frac{P}{\pi} \sin^{-1} \left[\sqrt{\frac{(1+k)^2 - b_\lambda^2}{a_\lambda^2 - b_\lambda^2}} \right], \quad (\text{A3})$$

$$T_{\text{full}} = \frac{P}{\pi} \sin^{-1} \left[\sqrt{\frac{(1-k)^2 - b_\lambda^2}{a_\lambda^2 - b_\lambda^2}} \right], \quad (\text{A4})$$

where arguments for λ are omitted for readability. In contrast, the duration T_c during which the center of the planetary shadow transits the host star is

$$T_c = \frac{P}{\pi} \sin^{-1} \left[\sqrt{\frac{1 - b_\lambda^2}{a_\lambda^2 - b_\lambda^2}} \right]. \quad (\text{A5})$$

Thus, $T_c \neq (T_{\text{tot}} + T_{\text{full}})/2$, meaning $t'_i = t_0 - T_c/2 \neq t_i$ and $t'_e = t_0 + T_c/2 \neq t_e$. For WASP-39 b, assuming $P = 4$ days, $k = 0.145$, $a = 11.4 R_s$, and $b = 0.45$, we find $T_c - (T_{\text{tot}} + T_{\text{full}})/2 \sim 30$ s and $t_i - t'_i \sim -15$ s.

Additionally, if the planetary atmosphere is perfectly symmetric, T_c corresponds to the transit duration for the center of mass of the planet, T_{bc} . In §4, we approximated T_{bc} using $(T_{\text{tot}} + T_{\text{full}})/2$, even though $T_c \neq (T_{\text{tot}} + T_{\text{full}})/2$. While this approximation has a negligible impact on current data when estimating wavelength dependence alone, adjustments may be needed as data precision improves.

B. STELLAR RADII BASED ON A STELLAR ATMOSPHERIC MODEL

In the formulation, the wavelength dependence of the host star’s radius, denoted as $\alpha(\lambda)$, is taken into account. Simulations based on a stellar atmospheric model suggest a wavelength-dependent variation in stellar radii. Figure 27 shows the normalized specific intensities of a star with an effective temperature of 5500 K, surface gravity $\log g$ [cgs] = 4.5, and metallicity [Fe/H] = 0.0, computed by Husser et al. (2013) using the spherically symmetric model of PHOENIX. The horizontal axis represents $\mu = \cos \theta$, where θ is the angle between the line of sight and the normal to the stellar surface. The figure shows that the μ value at which the intensity begins to drop sharply increases with wavelength. Figure 28 illustrates the variation of $\mu_{0.5}$, defined as the μ value where the specific intensity satisfies $I(\mu) = I(1)/2$, across different wavelengths. These values were calculated using specific intensities binned into 5 nm intervals. Assuming $\mu_{0.5}$ as the stellar limb, the stellar radius is found to change at a rate of approximately $0.12\% \mu\text{m}^{-1}$ within the wavelength range of 3 to 5 μm .

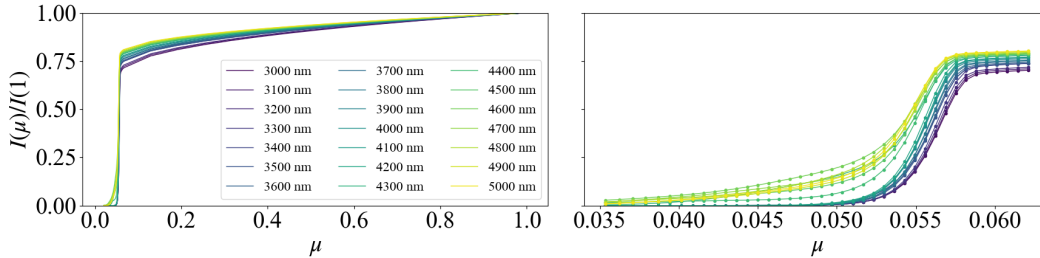


Figure 27. Normalized specific intensities of a star with an effective temperature of 5500 K, $\log g$ [cgs] = 4.5, and metallicity [Fe/H] = 0.0, computed by Husser et al. (2013) using the spherically symmetric model of PHOENIX. The right panel provides a magnified view around the μ value where the intensity begins to drop sharply.

C. ALTERNATIVE DATA REDUCTION AND COMPARISON OF SPECTRA

To verify the impact of data reduction on the resulting spectra, an alternative data reduction process, different from that described in §4.1, was performed. Hereafter, we refer to the data reduction described in §4.1 as “Reduction A” and the alternative process as “Reduction B.” This process primarily follows the approach applied to the data labeled “ExoTiC-JEDI [V1]” in Alderson et al. (2023). The ExoTiC-JEDI pipeline (Alderson et al. 2023) was used for Reduction B, with some necessary customizations.

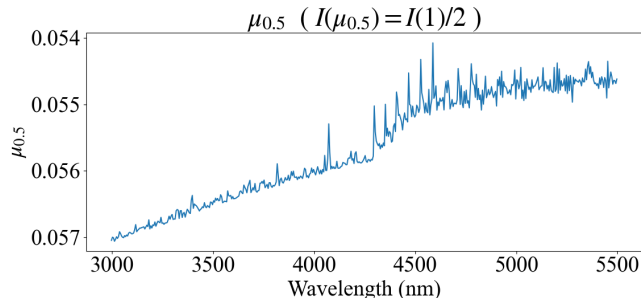


Figure 28. Variation of $\mu_{0.5}$, defined as the μ value where the specific intensity satisfies $I(\mu) = I(1)/2$, across different wavelengths. These values were calculated using the specific intensities of a star with an effective temperature of 5500 K, $\log g$ [cgs] = 4.5, and metallicity [Fe/H] = 0.0, computed by [Husser et al. \(2013\)](#) using the spherically symmetric model of PHOENIX, and binned into 5 nm intervals.

To obtain the spectral time series, we first used stages 1 of the ExoTiC-JEDI pipeline ([Alderson et al. 2023](#)). Stage 1 closely followed the JWST pipeline ([Bushouse et al. 2024](#)), with the addition of a group-level destriping step as described in [Alderson et al. \(2023\)](#). In Reduction B, the bias subtraction step of the JWST pipeline was used. The ramp-jump detection threshold was set to the default value of 4σ , and all other settings were kept at their defaults, either as determined by the JWST pipeline ([Bushouse et al. 2024](#)) or specified in [Alderson et al. \(2023\)](#) for the group-level destriping step.

The resulting data was processed following [Alderson et al. \(2023\)](#). We utilized the data-quality flags generated by the JWST Calibration Pipeline to identify problematic pixels, including those flagged as bad, saturated, dead, hot, or exhibiting low quantum efficiency or missing gain values. These pixels were replaced with the median value of their surrounding pixels. Additionally, we performed a search within each integration to identify spatial outliers, defined as pixels deviating from the median of the surrounding 20 pixels in the same row by more than 6σ , and temporal outliers, defined as pixels differing from the median of that pixel across the surrounding ten integrations by more than 20σ . Any detected outliers were replaced with the corresponding median values. To determine the trace position and width, we fitted a Gaussian to each column within an integration. A fourth-order polynomial was then applied to the trace centers and standard deviations values, smoothed using a median filter, to define the aperture region. This aperture extended vertically by five standard deviations from the center of the trace. For background subtraction, the median value of the unilluminated region in each column was subtracted, excluding pixels located within five pixels of the aperture. For each integration, the pixel counts within the aperture region were summed across columns using an intrapixel extraction method. This process yielded 1D stellar spectra for each integration, with uncertainties calculated based on photon noise and readout noise.

We obtained the spectra of R_p^{xe-} , R_p^{xi+} , R_p^{xi-} , and R_p^{xe+} using the procedure described in §4. Figure 29 shows these spectra (colored dots) alongside those obtained with Reduction A (gray dots). The spectral shapes derived from both reductions are nearly identical, with only minor differences. Small offsets are observed between them, which result from differences in the orbital parameters estimated through MCMC sampling for wavelengths corresponding to radii smaller than the 10th percentile. Since two independent procedures produced nearly identical spectra, we consider the reduction process to be reliable.

D. DISCUSSION OF LIMB DARKENING COEFFICIENTS PARAMETRIZATION AND WAVELENGTH DEPENDENCE

In §4, we used a quadratic limb darkening model with q_1 and q_2 values from [Kipping \(2013\)](#). Regarding the parameterization of limb darkening coefficients, [Coulombe et al. \(2024\)](#) demonstrated that using q_1 and q_2 could introduce wavelength-dependent biases in the inferred transit depths. To investigate this issue, we performed additional light curve fits with free u_1 and u_2 for each wavelength, and compared the results with those in §4. In this analysis, we employed a wide uniform prior distribution $\mathcal{U}(-3, 3)$ for both u_1 and u_2 , while keeping all other settings and procedures the same as those in §4.

Figure 30 shows the inferred values of all the parameters in the light curve model obtained from the MCMC sampling (gray dots), along with those inferred in §4 assuming a linear wavelength dependence for q_1 and q_2 (blue

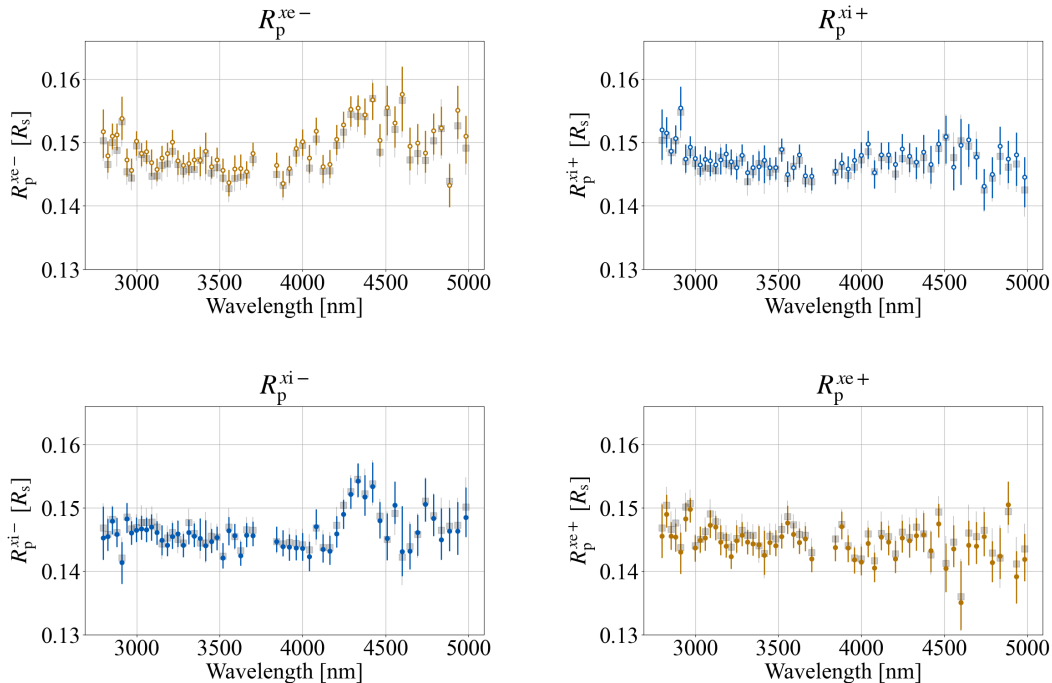


Figure 29. Spectra of R_p^{xe-} (top left), R_p^{xi+} (top right), R_p^{xi-} (bottom left), and R_p^{xe+} (bottom right). The dots with error bars represent the median values from the MCMC sampling with 68% credible intervals. The colored dots indicate the Reduction B, while the gray dots indicate the Reduction A.

dots). While the uncertainties increased, we found that almost all parameters remained consistent with the results from §4. Furthermore, we did not detect the wavelength-dependent biases in the inferred transit depth k^2 , which were reported by Coulombe et al. (2024) when using the q_1 and q_2 parameterization. These biases tend to reduce the inferred transit depth. This absence of bias could be due to the low resolution of the spectra analyzed here, which are typically of higher precision, as noted by Coulombe et al. (2024). Therefore, we conclude that using the q_1 and q_2 parameterization does not introduce problems in the analysis presented in §4.

To investigate how different treatments of the limb darkening coefficients affect the results, we obtained the spectra of R_p^{xe-} , R_p^{xi+} , R_p^{xi-} , and R_p^{xe+} (Figure 31). For clarity, we used the orbital parameters of the planet’s center of mass estimated in §4, to isolate the effect of the limb darkening treatment on the shape of the spectra. While the uncertainties in the resulting spectra were larger, the overall shape remained consistent with the results obtained using a linear wavelength dependence for q_1 and q_2 , including absorption features around 4 to 4.5 μm on the evening side. Even when assuming the extreme case of no wavelength dependence for u_1 and u_2 , the general shape of the spectra still agrees. This suggests that assuming a simple linear wavelength dependence for q_1 and q_2 does not significantly distort the overall shape of the spectra.

REFERENCES

- Agol, E., Luger, R., & Foreman-Mackey, D. 2020, *AJ*, 159, 123, doi: [10.3847/1538-3881/ab4fee](https://doi.org/10.3847/1538-3881/ab4fee)
- Agúndez, M., Parmentier, V., Venot, O., Hersant, F., & Selsis, F. 2014, *A&A*, 564, A73, doi: [10.1051/0004-6361/201322895](https://doi.org/10.1051/0004-6361/201322895)
- Al Derzi, A. R., Furtenbacher, T., Tennyson, J., Yurchenko, S. N., & Császár, A. G. 2015, *JQSRT*, 161, 117, doi: [10.1016/j.jqsrt.2015.03.034](https://doi.org/10.1016/j.jqsrt.2015.03.034)
- Alderson, L., Grant, D., & Wakeford, H. 2022, Exo-TiC/ExoTiC-JEDI: v0.1-beta-release, v0.1, Zenodo, doi: [10.5281/zenodo.7185855](https://doi.org/10.5281/zenodo.7185855)
- Alderson, L., Wakeford, H. R., Alam, M. K., et al. 2023, *Nature*, 614, 664, doi: [10.1038/s41586-022-05591-3](https://doi.org/10.1038/s41586-022-05591-3)
- Azzam, A. A. A., Tennyson, J., Yurchenko, S. N., & Naumenko, O. V. 2016, *MNRAS*, 460, 4063, doi: [10.1093/mnras/stw1133](https://doi.org/10.1093/mnras/stw1133)

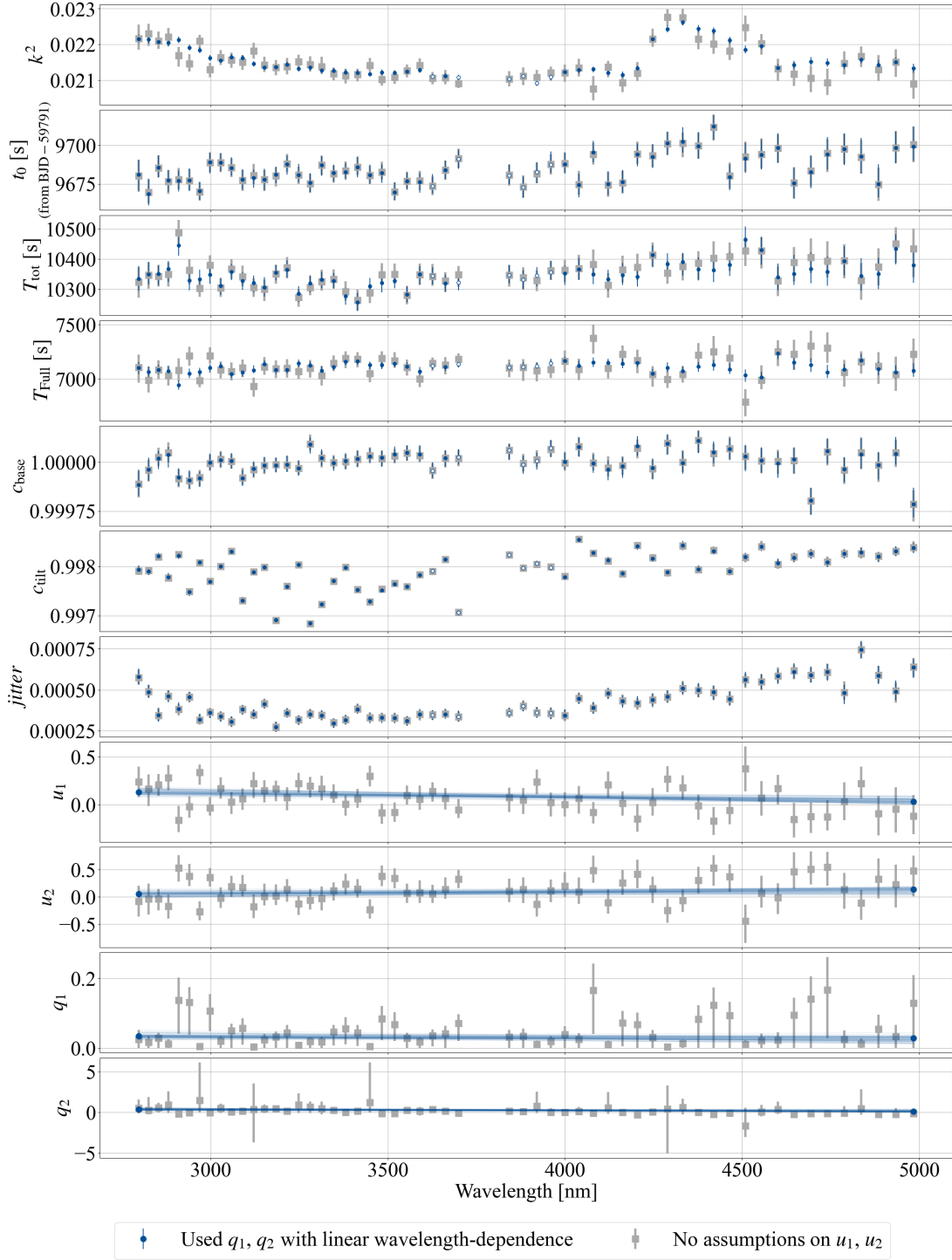


Figure 30. Inferred values of all the parameters in the light curve model obtained from the MCMC sampling. The gray dots represent the results using free u_1 and u_2 for each wavelength, while the blue dots represent the results assuming a linear wavelength dependence for q_1 and q_2 in the MCMC analysis. For the limb darkening coefficients inferred using the assumption of a linear wavelength dependence for q_1 and q_2 , the inferred values at the minimum and maximum wavelengths, as well as the wavelength dependence for each sampling, are shown. The dots indicate the median values of the MCMC sampling, and the error bars represent the 68% credible intervals.

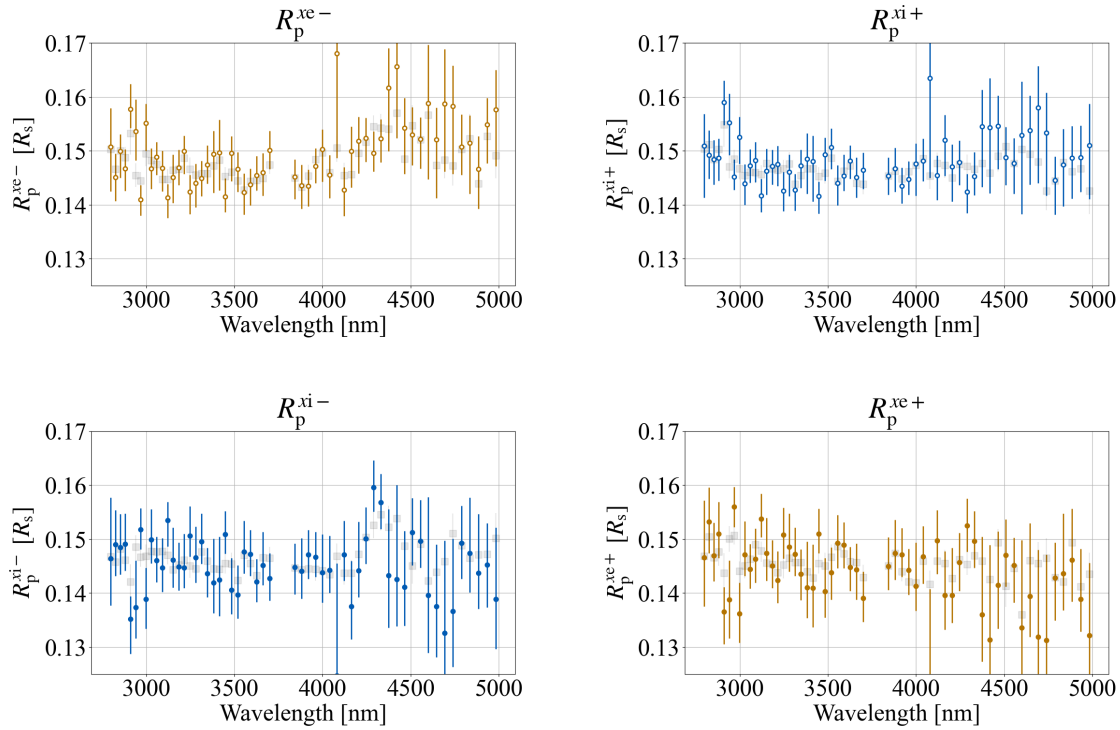


Figure 31. Spectra of R_p^{xe-} (top left), R_p^{xi+} (top right), R_p^{xi-} (bottom left), and R_p^{xe+} (bottom right). The dots with error bars represent the median values from the MCMC sampling, with 68% credible intervals. The colored dots indicate the results using free u_1 and u_2 for each wavelength, while the gray dots indicate the results assuming a linear wavelength dependence for q_1 and q_2 in the MCMC analysis.

Bingham, E., Chen, J. P., Jankowiak, M., et al. 2019, *J. Mach. Learn. Res.*, 20, 28:1.

<http://jmlr.org/papers/v20/18-403.html>

Böker, T., Beck, T. L., Birkmann, S. M., et al. 2023, *PASP*, 135, 038001, doi: [10.1088/1538-3873/acb846](https://doi.org/10.1088/1538-3873/acb846)

Bradbury, J., Frostig, R., Hawkins, P., et al. 2018, *JAX: composable transformations of Python+NumPy programs*, 0.4.28. <http://github.com/google/jax>

Bushouse, H., Eisenhamer, J., Dencheva, N., et al. 2024, *JWST Calibration Pipeline*, 1.14.0, Zenodo, doi: [10.5281/zenodo.10870758](https://doi.org/10.5281/zenodo.10870758)

Charròn, M., Anderson, T. G., & Steinfeld, J. I. 1980, *JChPh*, 73, 1494, doi: [10.1063/1.440354](https://doi.org/10.1063/1.440354)

Chubb, K. L., Tennyson, J., & Yurchenko, S. N. 2020, *MNRAS*, 493, 1531, doi: [10.1093/mnras/staa229](https://doi.org/10.1093/mnras/staa229)

Chubb, K. L., Naumenko, O., Keely, S., et al. 2018, *JQSRT*, 218, 178, doi: [10.1016/j.jqsrt.2018.07.012](https://doi.org/10.1016/j.jqsrt.2018.07.012)

Cohen, J. B., & Wilson, E. B. 1973, *JChPh*, 58, 442, doi: [10.1063/1.1679224](https://doi.org/10.1063/1.1679224)

Coles, P. A., Yurchenko, S. N., & Tennyson, J. 2019, *MNRAS*, 490, 4638, doi: [10.1093/mnras/stz2778](https://doi.org/10.1093/mnras/stz2778)

Constantinou, S., & Madhusudhan, N. 2024, *MNRAS*, 530, 3252, doi: [10.1093/mnras/stae633](https://doi.org/10.1093/mnras/stae633)

Coulombe, L.-P., Roy, P.-A., & Benneke, B. 2024, *AJ*, 168, 227, doi: [10.3847/1538-3881/ad7aef](https://doi.org/10.3847/1538-3881/ad7aef)

Dobbs-Dixon, I., & Agol, E. 2013, *MNRAS*, 435, 3159, doi: [10.1093/mnras/stt1509](https://doi.org/10.1093/mnras/stt1509)

Dobbs-Dixon, I., Agol, E., & Burrows, A. 2012, *ApJ*, 751, 87, doi: [10.1088/0004-637X/751/2/87](https://doi.org/10.1088/0004-637X/751/2/87)

Emilio, M., Couvidat, S., Bush, R. I., Kuhn, J. R., & Scholl, I. F. 2015, *ApJ*, 798, 48, doi: [10.1088/0004-637X/798/1/48](https://doi.org/10.1088/0004-637X/798/1/48)

Emilio, M., Kuhn, J. R., Bush, R. I., & Scholl, I. F. 2012, *ApJ*, 750, 135, doi: [10.1088/0004-637X/750/2/135](https://doi.org/10.1088/0004-637X/750/2/135)

Esparza-Borges, E., López-Morales, M., Adams Redai, J. I., et al. 2023, *ApJL*, 955, L19, doi: [10.3847/2041-8213/acf27b](https://doi.org/10.3847/2041-8213/acf27b)

Espinoza, N., & Jones, K. 2021, *AJ*, 162, 165, doi: [10.3847/1538-3881/ac134d](https://doi.org/10.3847/1538-3881/ac134d)

Espinoza, N., Steinrueck, M. E., Kirk, J., et al. 2024, *Nature*, 632, 1017, doi: [10.1038/s41586-024-07768-4](https://doi.org/10.1038/s41586-024-07768-4)

Faedi, F., Barros, S. C. C., Anderson, D. R., et al. 2011, *A&A*, 531, A40, doi: [10.1051/0004-6361/201116671](https://doi.org/10.1051/0004-6361/201116671)

Falco, A., Leconte, J., Mechineau, A., & Pluriel, W. 2024, *A&A*, 685, A125, doi: [10.1051/0004-6361/202348880](https://doi.org/10.1051/0004-6361/202348880)

- Fleury, B., Gudipati, M. S., Henderson, B. L., & Swain, M. 2020, *ApJ*, 899, 147, doi: [10.3847/1538-4357/aba828](https://doi.org/10.3847/1538-4357/aba828)
- Foreman-Mackey, D., Luger, R., Agol, E., et al. 2021, *The Journal of Open Source Software*, 6, 3285, doi: [10.21105/joss.03285](https://doi.org/10.21105/joss.03285)
- Fortney, J. J., Shabram, M., Showman, A. P., et al. 2010, *ApJ*, 709, 1396, doi: [10.1088/0004-637X/709/2/1396](https://doi.org/10.1088/0004-637X/709/2/1396)
- Gandhi, S., Kesseli, A., Snellen, I., et al. 2022, *MNRAS*, 515, 749, doi: [10.1093/mnras/stac1744](https://doi.org/10.1093/mnras/stac1744)
- Gordon, I. E., Rothman, L. S., Hill, C., et al. 2017, *JQSRT*, 203, 3, doi: [10.1016/j.jqsrt.2017.06.038](https://doi.org/10.1016/j.jqsrt.2017.06.038)
- Grant, D., & Wakeford, H. R. 2023, *MNRAS*, 519, 5114, doi: [10.1093/mnras/stac3632](https://doi.org/10.1093/mnras/stac3632)
- Grant, D., Lothringer, J. D., Wakeford, H. R., et al. 2023, *ApJL*, 949, L15, doi: [10.3847/2041-8213/acd544](https://doi.org/10.3847/2041-8213/acd544)
- Gregory, P. C. 2005, *Bayesian Logical Data Analysis for the Physical Sciences: A Comparative Approach with ‘Mathematica’ Support*
- Hargreaves, R. J., Gordon, I. E., Rey, M., et al. 2020, *ApJS*, 247, 55, doi: [10.3847/1538-4365/ab7a1a](https://doi.org/10.3847/1538-4365/ab7a1a)
- Harris, C. R., Millman, K. J., van der Walt, S. J., et al. 2020, *Nature*, 585, 357, doi: [10.1038/s41586-020-2649-2](https://doi.org/10.1038/s41586-020-2649-2)
- Harris, G. J., Tennyson, J., Kaminsky, B. M., Pavlenko, Y. V., & Jones, H. R. A. 2006, *MNRAS*, 367, 400, doi: [10.1111/j.1365-2966.2005.09960.x](https://doi.org/10.1111/j.1365-2966.2005.09960.x)
- Hattori, S., Garcia, L., Murray, C., et al. 2024, *exoplanet-dev/jaxoplanet: Astronomical time series analysis with JAX, v0.0.2, Zenodo*, doi: [10.5281/zenodo.10736936](https://doi.org/10.5281/zenodo.10736936)
- Hoyer, S., Roos, M., Joseph, H., et al. 2024, *xarray, v2024.03.0, Zenodo*, doi: [10.5281/zenodo.10895413](https://doi.org/10.5281/zenodo.10895413)
- Hunter, J. D. 2007, *Computing in Science & Engineering*, 9, 90, doi: [10.1109/MCSE.2007.55](https://doi.org/10.1109/MCSE.2007.55)
- Husser, T. O., Wende-von Berg, S., Dreizler, S., et al. 2013, *A&A*, 553, A6, doi: [10.1051/0004-6361/201219058](https://doi.org/10.1051/0004-6361/201219058)
- Jakobsen, P., Ferruit, P., Alves de Oliveira, C., et al. 2022, *A&A*, 661, A80, doi: [10.1051/0004-6361/202142663](https://doi.org/10.1051/0004-6361/202142663)
- Jones, K., & Espinoza, N. 2020, *The Journal of Open Source Software*, 5, 2382, doi: [10.21105/joss.02382](https://doi.org/10.21105/joss.02382)
- Kammer, J. A., Knutson, H. A., Line, M. R., et al. 2015, *ApJ*, 810, 118, doi: [10.1088/0004-637X/810/2/118](https://doi.org/10.1088/0004-637X/810/2/118)
- Karman, T., Gordon, I. E., van der Avoird, A., et al. 2019, *Icarus*, 328, 160, doi: [10.1016/j.icarus.2019.02.034](https://doi.org/10.1016/j.icarus.2019.02.034)
- Kawahara, H., Kawashima, Y., Masuda, K., et al. 2022, *ApJS*, 258, 31, doi: [10.3847/1538-4365/ac3b4d](https://doi.org/10.3847/1538-4365/ac3b4d)
- Kempton, E. M. R., Bean, J. L., & Parmentier, V. 2017, *ApJL*, 845, L20, doi: [10.3847/2041-8213/aa84ac](https://doi.org/10.3847/2041-8213/aa84ac)
- Kipping, D. M. 2013, *MNRAS*, 435, 2152, doi: [10.1093/mnras/stt1435](https://doi.org/10.1093/mnras/stt1435)
- Kokori, A., Tsiaras, A., Edwards, B., et al. 2023, *ApJS*, 265, 4, doi: [10.3847/1538-4365/ac9da4](https://doi.org/10.3847/1538-4365/ac9da4)
- Line, M. R., & Parmentier, V. 2016, *ApJ*, 820, 78, doi: [10.3847/0004-637X/820/1/78](https://doi.org/10.3847/0004-637X/820/1/78)
- Mancini, L., Esposito, M., Covino, E., et al. 2018, *A&A*, 613, A41, doi: [10.1051/0004-6361/201732234](https://doi.org/10.1051/0004-6361/201732234)
- Mehrotra, S. C., Mäder, H., de Vreede, J. P. M., & Dijkerman, H. A. 1985, *Chemical Physics*, 93, 115, doi: [10.1016/0301-0104\(85\)85053-9](https://doi.org/10.1016/0301-0104(85)85053-9)
- Millan-Gabet, R., Pedretti, E., Monnier, J. D., et al. 2005, *ApJ*, 620, 961, doi: [10.1086/427163](https://doi.org/10.1086/427163)
- Murphy, M. M., Beatty, T. G., Schlawin, E., et al. 2024, *Nature Astronomy*, doi: [10.1038/s41550-024-02367-9](https://doi.org/10.1038/s41550-024-02367-9)
- Phan, D., Pradhan, N., & Jankowiak, M. 2019, *arXiv e-prints*, arXiv:1912.11554, doi: [10.48550/arXiv.1912.11554](https://doi.org/10.48550/arXiv.1912.11554)
- Phan, D., Pradhan, N., & Jankowiak, M. 2019, *arXiv preprint arXiv:1912.11554*
- Powell, D., Feinstein, A. D., Lee, E. K. H., et al. 2024, *Nature*, 626, 979, doi: [10.1038/s41586-024-07040-9](https://doi.org/10.1038/s41586-024-07040-9)
- Richard, C., Gordon, I. E., Rothman, L. S., et al. 2012, *JQSRT*, 113, 1276, doi: [10.1016/j.jqsrt.2011.11.004](https://doi.org/10.1016/j.jqsrt.2011.11.004)
- Rothman, L. S., Gordon, I. E., Barber, R. J., et al. 2010, *JQSRT*, 111, 2139, doi: [10.1016/j.jqsrt.2010.05.001](https://doi.org/10.1016/j.jqsrt.2010.05.001)
- Rothman, L. S., Gordon, I. E., Babikov, Y., et al. 2013, *JQSRT*, 130, 4, doi: [10.1016/j.jqsrt.2013.07.002](https://doi.org/10.1016/j.jqsrt.2013.07.002)
- Rozelot, J.-P., Kosovichev, A., & Kilcik, A. 2016, in *IAU Symposium, Vol. 320, Solar and Stellar Flares and their Effects on Planets*, ed. A. G. Kosovichev, S. L. Hawley, & P. Heinzel, 342–350, doi: [10.1017/S1743921316002118](https://doi.org/10.1017/S1743921316002118)
- Rustamkulov, Z., Sing, D. K., Mukherjee, S., et al. 2023, *Nature*, 614, 659, doi: [10.1038/s41586-022-05677-y](https://doi.org/10.1038/s41586-022-05677-y)
- Sarkar, S., Madhusudhan, N., Constantinou, S., & Holmberg, M. 2024, *MNRAS*, 531, 2731, doi: [10.1093/mnras/stae1230](https://doi.org/10.1093/mnras/stae1230)
- Stevenson, K. B., Lewis, N. K., Bean, J. L., et al. 2016, *PASP*, 128, 094401, doi: [10.1088/1538-3873/128/967/094401](https://doi.org/10.1088/1538-3873/128/967/094401)
- Tóbiás, R., Furtenbacher, T., Császár, A. G., et al. 2018, *JQSRT*, 208, 152, doi: [10.1016/j.jqsrt.2018.01.006](https://doi.org/10.1016/j.jqsrt.2018.01.006)
- Tsai, S.-M., Moses, J. I., Powell, D., & Lee, E. K. H. 2023a, *ApJL*, 959, L30, doi: [10.3847/2041-8213/ad1405](https://doi.org/10.3847/2041-8213/ad1405)
- Tsai, S.-M., Lee, E. K. H., Powell, D., et al. 2023b, *Nature*, 617, 483, doi: [10.1038/s41586-023-05902-2](https://doi.org/10.1038/s41586-023-05902-2)
- Underwood, D. S., Tennyson, J., Yurchenko, S. N., et al. 2016, *MNRAS*, 459, 3890, doi: [10.1093/mnras/stw849](https://doi.org/10.1093/mnras/stw849)
- von Paris, P., Gratier, P., Bordé, P., Leconte, J., & Selsis, F. 2016, *A&A*, 589, A52, doi: [10.1051/0004-6361/201527894](https://doi.org/10.1051/0004-6361/201527894)

Wilzewski, J. S., Gordon, I. E., Kochanov, R. V., Hill, C.,
& Rothman, L. S. 2016, JQSRT, 168, 193,
doi: [10.1016/j.jqsrt.2015.09.003](https://doi.org/10.1016/j.jqsrt.2015.09.003)

Winn, J. N. 2010, in Exoplanets, ed. S. Seager, 55–77,
doi: [10.48550/arXiv.1001.2010](https://doi.org/10.48550/arXiv.1001.2010)
Wittkowski, M., Boboltz, D. A., Driebe, T., et al. 2008,
A&A, 479, L21, doi: [10.1051/0004-6361:20079237](https://doi.org/10.1051/0004-6361:20079237)